UC Berkeley
UC Berkeley Electronic Theses and Dissertations

Title
Bioluminescence imaging of hepatic nutrient fluxes

Permalink
https://escholarship.org/uc/item/3t92c2fp

Author
Park, Hyo Min

Publication Date
2016

Peer reviewed|Thesis/dissertation

Bioluminescence imaging of hepatic nutrient fluxes

By

Hyo Min Park

A dissertation submitted in partial satisfaction of the

requirements for the degree of

Doctor of Philosophy

in

Metabolic Biology

in the

Graduate Division

of the

University of California, Berkeley

Committee in charge:

Professor Andreas Stahl, Chair
Professor Hei Sook Sul
Professor Jen-Chywan Wang
Professor George A. Brooks

Summer 2016

Bioluminescence imaging of hepatic nutrient fluxes

©2016

by Hyo Min Park

Abstract

Bioluminescence imaging of hepatic nutrient fluxes

by

Hyo Min Park

Doctor of Philosophy in Metabolic Biology

University of California, Berkeley

Professor Andreas Stahl, Chair

Bioluminescence imaging (BLI) is a powerful technology for studying molecular and cellular features in living animals. Impressive advances in luciferase engineering and ease of targeting by genetic encoding permit the broad use of bioluminescence for in vivo imaging for diverse purposes. First, we generated transgenic mice with liver-specific expression of luciferase and used BLI with a FFA probe to enable non-invasive real-time imaging of FFA flux in the liver. Our approach enabled us to observe the changes in FFA hepatic uptake under different physiological conditions in live animals. We found that our novel imaging system is a useful and reliable tool to study the dynamic changes in hepatic FFA flux in preclinical model systems.

We also utilize this imaging approach to study the role of fatty acid transport proteins in hepatic carcinogenesis. We generated a genetically engineered liver cancer mouse model via hydrodynamic transfection and determined the changes of fatty acid uptake during tumor formation. Our results demonstrated that the rate of FFA uptake is significantly decreased during the development of hepatocellular carcinoma (HCC), but not that of intrahepatic cholangiocarcinoma (ICC). We additionally showed that FATP5 knockdown suppresses ICC tumor formation and that the down regulation of FATP5 expression delays tumor growth even after the onset of ICC. These findings uncovered the critical role of FATP5 in ICC development and demonstrated the potential utility of these proteins as therapeutic targets for the prevention and treatment of ICC.

We expanded our bioluminescent imaging approaches to other nutrients and copper in particular. We demonstrated Copper-Caged Luciferin-1 (CCL-1), a bioluminescent copper-responsive probe can detect physiological changes in labile Cu^+ levels in live cells and mice under situations of copper deficiency or overload. Application of CCL-1 to mice with liver-specific luciferase expression in a diet-induced model of non-alcoholic fatty liver disease (NAFLD) reveals onset of hepatic copper

deficiency and altered expression levels of central copper trafficking proteins that accompany symptoms of glucose intolerance and weight gain.

Lastly, we also utilized bioluminescent approaches to detect liver damage and apoptosis. We shown that D-cysteine and 2-cyanobenzothiazoles can selectively react with each other in vivo to generate a luciferin substrate for firefly luciferase. We applied this "split luciferin" ligation reaction to the imaging of apoptosis associated with caspase 3/7. Importantly, this strategy was found to be superior to the commercially available DEVD-aminoluciferin substrate for imaging of caspase 3/7 activity. Moreover, the split luciferin approach enables the modular construction of bioluminogenic sensors, where either or both reaction partners could be caged to report on multiple biological events. These imaging approaches for nutrient fluxes should open up our understandings of complex metabolic networks in various metabolic processes and diseases states.

Dedicated to

Father and Mother

Minsun and Chloe, TJ, Claire

Your inexhaustible love and support

Table of Contents

List of figures

Acknowledgements

Graduate school has been the most exciting and wonderful learning experience in my entire life. I would not be where I am today without the help of all the people around me.

First, I would like to thank my advisor Professor Andreas Stahl. Andreas has always been a very supportive and patient mentor. His door is always open, and he has never hesitated to provide help and guidance when I was lost. From him, I have learned how to properly design experiments and think critically about my results. I am truly grateful for the countless hours he spent meeting with me throughout my time here. Without a doubt, I am positive that the skills I have learned from him will be invaluable in my future career as a scientist.

Next, I would like to acknowledge all of the Stahl Lab members for their help and guidance over the years. Ching Feng, Brittney, Lacey, Kevin, were always there for support whenever I had questions or help about anything. I would also like to thank all of my past labmates, Biao, Courtney, Mellisa, Rost, Amy who taught me a lot more than I could ever imagine.

I would also like to acknowledge the other people I have worked and collaborated with during my graduate research. I would like to thank Professor Elena A. Dubikovskaya and Aurélien Godinat for conducting the in vitro and in vivo experiments in split luciferin ligation study. They have been great collaborators, and I have learned a lot about chemistry while I worked with them. I would like to thank Dr. Marie Heffern who conducted all the experiments with copper probe. While I worked with her, I learned a lot about chemistry and was highly impressed with her enthusiasm for science.

I would like to give special thanks to my dissertation committee. I owe a debt of gratitude to Professor Hei Sook Sul, who encouraged me to pursue this degree and mentored me from my qualifying exam. I must also thank Professor Jen-Chywan Wang for his time and careful attention to detail. To Professor George A. Brooks, thank you for your kind mentoring, and I learned a lot in your classes about scientific presentation and way of thinking and interpreting scientific data.

I would also like to thank my family for always being there for me. I am truly grateful for our unconditional love and support. Mom and Dad, your belief in me has helped me to achieve my dreams. I appreciate all that you have given me and continue to give to me. I must thank to my father-in-law and mother-in-law for their endless support and belief.

To my beloved kids Chloe, TJ and Claire. I would like to express my thanks for being such good kids and always cheering me up. You all bring joy and excitement into my life. I love you all, and I hope all of you will grow up to be smart and beautiful people who

make a significant impact in society. I believe in you, and I know that I am and will always be your number one supporter

Finally and most importantly, I would like to thank my wife, Minsun Lee. I truly would not be who I am today without her. Her support, encouragement, patience and unwavering love were undeniably the bedrock upon which the past ten years of my life have been built upon. I am so sorry for not being the most attentive husband, but I hope she knows that I'm the one who loves her the most in the world.

Chapter 1

General introduction

Bioluminescence imaging

Many imaging strategies have been developed and refined in order to observe biological processes in living mammals as they are happening in real time. These imaging techniques enable diverse biological features to be visualized, which furthers our understanding of various of biomolecular functions[1]. Within the past decade, there has been a rapid growth in bioluminescent imaging (BLI) applications because of the advantages of BLI in living animals, which include high sensitivity, relatively low cost, and ease of operation[2, 3].

Bioluminescence is defined as the emission of light produced by enzymatic reactions in living organisms and is used in nature for various purposes, including disguise for luring prey, signaling for courtship and mating, or hiding from predators[4-6]. Dubois first found that bioluminescence occurred due to the luciferin-luciferase reaction in the luminescent beetle Pyrophorus in 1885[7]. In general, light in bioluminescence is produced by a chemical reaction involving a combination of two types of substances: luciferin, a light-producing substance, and luciferase, an enzyme that catalyzes the reaction. Luciferase binds its cognate luciferin and catalyzes the oxidation of luciferin, in which the by-products of the reaction are photons. The light-producing process also requires the presence of other substances, such as oxygen and adenosine triphosphate(ATP)[8].

Since the initial discovery, many different luciferase-luciferin reactions have been identified. Moreover, as our understanding of bioluminescence has increased, BLI has emerged as a powerful tool for noninvasive visualization of molecular and cellular processes in live animals[3, 9, 10]. In 1995, bioluminescent light was first exploited for imaging *in vivo* in a study of pathogenic processes using bioluminescent *Salmonella*[11]. In this previous study, researchers determined the specific tissues that were infected by the bacterium and then monitored the progress of infections by quantifying the bioluminescent light signal. These findings showed that BLI has significant potential to become a promising *in vivo* imaging tool. Since then, many luciferases from different organisms have been incorporated into a variety of hosts, including transgenic animals, and have been exploited to construct bioassay systems for both basic science research and preclinical studies[9, 12].

Applications of BLI
Cell tracking

For *in vivo* imaging, a subset of luciferases has been introduced and validated as reporter genes in longitudinal studies. This allows us to track

migratory patterns in multiple cell types in live animal models for a variety of diseases[13]. Because of the relative ease of integrating reporter genes into tumor cell genomes, BLI has been tested for cell growth and tracking in neoplastic disease animal models[14]. For example, Edinger et al. used an immortalized cervical cancer cell line engineered to express a firefly luciferase gene and monitored the proliferation of these cells in irradiated severe combined immunodeficiency (SCID) mice[15]. Adams et al. identified human prostate cancer metastasis using a prostate-specific adenovirus vector expressing firefly luciferase, which was designed to be expressed specifically in prostate tumors. BLI revealed that the prostate cancer metastasized to the lung and spine[16]. Wetterwald et al. reported cancer metastasis to the bone marrow using BLI[17].

In addition to tumor studies, Bogt et al. used BLI to study cellular kinetics following the transplantation of bone marrow-derived mononuclear cells (MNCs) from transgenic mice express firefly luciferase (Fluc) and green fluorescence protein (GFP) in a mouse model of hindlimb ischemia[18]. *In vivo* BLI revealed cell migration to the injured limb after intravenous transplantation, and the majority of donor cell death was observed 4 weeks after intramuscular transplantation. The locations and survival durations of embryonic cardiomyoblasts after transplantation were monitored noninvasively using BLI by Wu et al[19]. Additionally, Hardy et al. provided evidence of the spatiotemporal trafficking patterns of lymphocytes within the body[20], and Beanau et al. used BLI to asses and track human neural progenitor cells (hNPCs) in the rat striatum[21]. The development of brighter luciferases through the combination of codon optimization, retroviral modification and improved labeling techniques for expression in various cell types has enabled for a more sensitive cell tracking in deeper tissues[22, 23]. For example, Rabinovich et al. engineered firefly luciferase encoded within a retrovial vector to generate detectable light that makes visualization of a very small of mouse T cells more than 100 times greater[22]. Moreover, Santos et al. developed a new approach that enabled the stable expression of luciferase in both mouse and human primary T cells, allowing for more sensitive cell tracking[23].

Gene expression

Regulation of gene expression is fundamental to cellular and molecular processes. Advances in genomic research have identified an increasing number of genes exhibiting aberrant expression in response to various physiological or pathological conditions[13]. BLI enables *in vivo* testing of conditional and spatiotemporal gene expression patterns in living animals. This is to elucidate the relevance of the genes, during the onset of the disease or in responses to various stimuli such as chemical stresses, in real time[24]. One of the most common applications of BLI is expressing the reporter gene from the promoter of a gene of interest or a gene placed under genetic elements

responsive to a certain desired transcription factor in order to test the effects of stimuli on gene expression. The expression of the luciferase protein is measured by photon flux and indicates the expression level of the target gene[9].

Bioluminescent reporters for gene expression have been used to study chemical toxicity[25], tumor hypoxia[26], circadian rhythm[27], heat-shock response[28], and genes involved in inflammation. For example, Ishikawa et al. generated a mouse strain in which the firefly luciferase reporter enzyme is expressed downstream of the chromosomal promoter of cyclooxygenase-2 (*Cox-2*) in order to induce luciferase expression in various organs. This mouse line enables the *in vivo* analysis of Cox-2 expression in many disease models[29]. Additionally, Keller et al. generated a reporter mouse model to visualize glial fibrillary acidic protein (GFAP) expression using a luciferase reporter and demonstrated the application of this mouse strain to evaluate amyotrophic lateral sclerosis progression[30]. Luo et al. utilized a luciferase gene fused to a promoter with multiple Smad-binding elements to show that Smad signaling is activated during neuronal degeneration in mice[31].

Protein stability

Several BLI strategies have been used to determine the function and stability of a target protein in biological events. One commonly used method to monitor protein stability is to fuse luciferase to the protein of interest. The stability of the target protein can be monitored by the bioluminescent output. For example, Lehmann et al. constructed a reporter vector containing luciferase and hypoxia inducible factor (HIF)-1α to study the stabilization of HIF-1α during tumor development using BLI *in vivo*. They stably transfected C51 murine cancer cells with a fusion reporter and injected the cells subcutaneously into nude mice to generate tumor allografts. BLI was used to measure HIF-1α-luciferase-induced bioluminescent signals, and the results revealed that HIF-1α was stabilized during the early phase of tumor development. However, it became unstable after the tumors reached a volume of 1 cm^3 [26].

In addition to monitoring the stability of a given protein, BLI has also enabled visualization of general protein degradation. For example, Moroz et al. developed luciferase reporter vectors and reporter cell lines to investigate both the stability and degradation of HIF-1α in normal and tumor cells[32]. The degradation rate of the reporter protein was determined by sequential bioluminescence measurements under different conditions.

Molecular probes for BLI

As mentioned above, BLI has been used in many applications. For more specific and accurate biological process imaging, bioluminescence probes that only react with a certain biological stimulus should be designed. BLI probes can be based on luciferase that are unable to perform the bioluminescence

enzymatic reaction until acted upon by the specific enzyme or molecule[33]. Also, caged luciferin, which cannot act as a substrate for the luciferase until it reacts with specific biological molecules, can also be a good BLI probe[34, 35].

Several activatable luciferases have been developed to sense enzymatic activities directly in living animals such as those of β-galactosidase[35], caspases[36-38], furin[39], and β-lactamases[40]. These probes take advantage of different techniques to turn on the light emission. For example, a luciferase probe in which the activity is silenced when fused with the estrogen receptor regulatory domain (ER) is widely used for apoptosis study. The ER domain was linked to the luciferase by a protease cleavage site for caspase-3 (DEVD). Upon cleavage, the ER domain is separated from the luciferase, allowing activation of bioluminescence which enables visualization and quantification of apoptosis in a non-invasive manner. This probe was useful for detecting apoptosis by BLI[37, 41].

There are only a couple of reported examples of luciferin derivatives that are activated by small molecules. These derivatives do not produce luminescence until an uncaging event has occurred. Henkin et al. created a bioactivatable molecular imaging probe based on long-chain fatty acids conjugated to luciferin[42]. The fatty acid was connected via a disulfide linker to luciferin as these linkers have been shown to be stable outside of cells even after injections into animals. Thus, free luciferin is only generated and measured following the disulfide linker's reduction, which then is followed by cyclization of the linker. Free luciferin is then converted by luciferase to oxyluciferin and a photon of light will be quantified to measure fatty acids uptake. Another probe, reported by the Chang group, is activated by a small molecule hydrogen peroxide[43]. This probe is a boronic acid-caged firefly luciferin molecule that selectively reacts with H_2O_2 to release firefly luciferin, which enables real-time detection of H_2O_2 within living animals.

Mouse models for liver cancer research

There are several types of liver cancer based on the original cell type of the cancer. Primary liver cancer and primary liver cancer is the sixth most common cancer and the third leading cause of cancer-related death worldwide[44]. The World Health Organization (WHO) estimated that the prevalence of liver cancer is approximately 30 cases per 100,000 individuals worldwide, with 782,000 new cases diagnosed in 2012[45]. There are four types of primary liver cancer: hepatocellular carcinoma (HCC), fibrolamellar HCC, intrahepatic cholangiocarcinoma (ICC), angiosarcoma. HCC is the most common type of cancer and accounts for approximately 80% of all primary liver cancers. Fibrolamellar carcinoma (FLC) is a rare sub type of HCC. Fibro refers to fibrous tissue and lamellar refers to the plate-like structure of the cells. It accounts for less than 1% of all primary liver cancers, but represents the majority of HCCs in young patients under 30 years of age and has conventionally been considered to

be a histologic variant of HCC[46, 47]. Angiosarcoma begins in the blood vessels of the liver and grow quickly. It is an extremely rare liver tumor that comprises of about 1 percent of all liver cancers[48]. ICC is the second most common primary liver cancer comprising of about 10% of all liver cancers; however, the incidence and mortality rate are increasing worldwide[49, 50]. Accordingly, various mouse models of liver cancer have been developed in order to improve our ability to diagnose, prevent, and treat this disease. However, each mouse model is only able to recapitulate some aspects of hepatocarcinogenesis, and no model is ideal for all research purposes.

Chemically induced hepatocarcinogenesis

Carcinogenesis can be induced experimentally by exposure to exogenous chemicals such as diethylnitrosamine(DEN), aflatoxine, carbon tetrachloride, and thioacetamide[51]. Among them, DEN is the most widely used chemical that has the potential to induce tumors in many organs including the liver, gastrointestinal tract and respiratory system[52]. Specifically in HCC, DEN alone is effective to induce a complete carcinogenesis.

In the liver, DEN is metabolized into α-hydroxylnitrosamine, which, in turn, spontaneously generates ethyldiazonium ion after a series of chemical reactions by enzymes of the cytochrome P450 family[52]. Such electrophilic agents attack DNA strands and lead to DNA adducts production[53]. Next, base excision and the repair of interstrand cross linking occurs to remove the DNA adducts. These processes are major factors in determining DEN carcinogenicity[54].

To induce HCC, DEN is typically administered to mice between 12 and 15 days of age by a single intraperitoneal (IP) injection of DEN in a nontoxic dose of 5ug/g of body weight[55, 56]. A single IP injection of high dose (90 ug/g body weight) also induced tumors in 5-week-old male C3H mice[57]. DEN-induced mouse models of HCC are predominantly used to study the molecular mechanisms of chemically induced hepatocarcinogenesis and establish a relationship between carcinogen exposure and specific genetic changes. Furthermore, this model can be used to evaluate the effects of chemicals that might prevent HCC development.

However, there are some problems concerning the chemically induced cancer model. Applying the results from the mouse studies to the human studies remains difficult[58] because of the inconsistencies between mouse and human carcinogenic risks. A few disadvantages of these models are the effects of sex, age and the genetic background of the mice on the predictability of HCC-development [59]. Also, the average time for forming a tumor is still quite long[60]. All in all, these shortcomings limit its use in preclinical studies.

Implantation models

Transplantation models are among the most frequently used models to induce HCC formation and it offers another strategy for cancer researchers to accomplish this task. The general concept is to implant HCC cell lines or fragments of tumors into nude or severe combined immune deficient (SCID) mice[61]. Implantation models are classified as allograft models or xenograft models based on whether the grafts and the recipients are from the same species[62].

Since the first report showed human tumor growth in immunodepressed mice[63], human tumor xenografts models have been widely used in preclinical studies due to their advantages which includes simple establishment and easy monitoring of the size of the tumor. Xenograft models are mostly utilized to discover potential tumor suppressing factors including new drugs or changes in gene expression[51]. Allograft models are frequently used for the immunotherapy studies for those who suffer from tumor recurrence[64]. In these cases, immunodeficient mice cannot be used and allograft models that use immunocompetent mice become the alternative. This is simply due to the fact that allograft models that the host immune system is normal, which means it more closely represents the nature of the tumor's micro-environment.

The implantation models can also be classified by their implantation location, which could either be an ectopic site or orthotopic site. Ectopic implantation of tumor cells or fragments usually occurs subcutaneously. Xenografts of human HCCs growing subcutaneously in mice are widely used in the preclinical evaluation of anticancer agents. The rapid development of tumors, the minimal labor that is required, the relative inexpensiveness and the ability to measure tumor size non-invasively are the main advantages of the ectopic, subcutaneous, application of grafts from human HCCs[65, 66].

Orthotopic implantation can be accomplished by intrahepatic implantation of tumor fragments or direct injection of tumor cells into the left hepatic lobe. With respect to tumor morphology, microenvironment, metastatic potential and the response to anticancer agents, these orthotopic implantation models mimic human HCCs more closely than that of the ectopic implantation[67, 68]. Furthermore, processes involved in local invasion, like angiogenesis, can be examined in their normal microenvironment[69].

Genetically engineered mouse models

Hundreds of genes are reported to undergo genetic alterations during liver cancer development[70, 71]. Thus it is critical to identify oncogenes that play key roles in hepatocarcinogenesis. Additionally, it is crucial to identify their partners that cooperatively activate oncogenic signaling pathways or inactivate tumor-suppressing pathways. Hence, genetically engineered mouse (GEM) models with alterations in candidate oncogenes or tumor suppressor genes can serve as a valuable tool for clarifying any gene contribution to hepatocarcinogenesis[72, 73].

Even though the exact genetic events during carcinogenesis are not completely understood, several cellular pathways such as p53, Rb and Wnt/β-catenin are known to be involved in hepatic tumor formation[74, 75]. Several recent transgenic mice lineages used to induce the formation of HCCs are transgenic in one of these pathways. For example, Simian Virus 40 T-antigen mice have been studied extensively. The genome of the simian virus 40 encodes two oncogenic proteins, the large and small T antigen. After infection, the large T antigen can cause malignant transformation of the host cell primarily by inactivating the tumor-suppressor genes *p53* and retinoblastoma protein[76, 77].

Kim et al. generated a HCC mouse model by placing the entire hepatitis B virus X(HBx) gene directly into the germline of mice under its own regulatory elements. Transgenic animals showed histopathological changes, specifically in the liver, and proceeded to the development of malignant carcinomas[78]. Moriya et al. generated transgenic mice containing the complete core gene of Hepatitis C virus (HCV) which is the main cause of HCC elucidating the role of the HCV in HCC development. After the age of 16 months, the mice developed hepatic tumors that initially appeared as adenomas containing fat droplets in the cytoplasm. Then HCC developed from within the adenomas. These results indicate that the transgenic mice carrying HCV core protein can be good animal models for determining the molecular events in hepatocarcinogenesis with HCV infection[79].

Although traditional GEM models have made a significant contribution to our understanding of the hepatocarcinogenesis, several shortcomings of the GEM model development limit its usage[80]. GEM generation requires high-cost, time-consuming processes such as microinjection of transgenes into pronuclei (for transgenic models), transfection and manipulation of embryonic stem cells (for knockout models), as well as implantation and subsequent breeding. Additionally, some oncogenes or tumor suppressor genes are critical for embryonic or fetal development, in which these genetic manipulations may lead to death during the embryonic period.

To overcome those shortcomings, several research groups employed a conditional and inducible system allowing the induction of somatic mutations in a tissue-specific and time-controlled manner[74, 75, 81]. In addition, a very novel and simple method for liver transgenesis has been recently developed[82, 83]. This method delivers naked DNA plasmids, which encode a gene of interest, into the liver via hydrodynamic transfection. This will be introduced in the next chapter.

Hydrodynamic injection

Each model system, ranging from xenografts to the most sophisticated GEMs, are limited in some way, so it is always necessary to develop new animal models for specific cancers such as ICC. Thus a novel method called hydrodynamic transfection, which combines hydrodynamic gene delivery and

Sleeping Beauty(SB) mediated somatic integration in mouse hepatocytes, is another option for liver cancer model generation[84].

The hydrodynamic gene delivery was first developed by Liu et al in 1999 for an efficient expression of exogenous genes in animals[82]. The standard procedure consists of a rapid tail vein injection of plasmid DNA in sterilized saline, equivalent to 10% of body weight. Such a large volume of DNA solution entering directly into the inferior vena cava stretches myocardial fibers over the optimal length for contraction, inducing cardiac congestion, and driving the injected solution into the liver in retrograde. As a consequence, the liver uptakes the most of the injected plasmid DNA in the body, and approximately 10% to 40% of hepatocytes can be transfected after hydrodynamic tail vein injection. Transfection efficiency in all other organs, including kidney, spleen, lung, and heart, is less than 0.1% of that of the liver[82]. After the injection, the transfected DNA is rapidly degraded in hepatocytes. However, to induce liver cancer, the genes need to be continuously expressed in hepatocytes. To overcome this critical technical challenge, SB transposase mediated somatic integration is utilized to enable long term gene expression in the liver[85-87]. Once the oncogene is stably expressed in mouse hepatocytes, this will eventually lead to tumor formation.

One of main advantages of the hydrodynamic transfection for liver cancer mouse model development in comparison to the traditional GEM is that it accelerates the speed of the experiments with relatively low cost. Also hydrodynamic transfection makes it easy to test multiple genes in tumor formation. Generally, tumor development requires the activation of multiple signaling pathways and, in many cases, the mutation of one gene is not sufficient to promote tumor formation. Thus the fact that we can test multiple genes' signaling pathway by just adding more plasmids is another big advantages of this novel technology. In addition, we can construct a reporter vector which includes a reporter gene conjugated with an oncogene to monitor tumor growth or tumor cell trafficking in a live mouse.

In general, because HCC development requires the activation of multiple signaling pathways, hydrodynamic transfection is a useful tool due to its ability to deliver multiple genes together. Ho et al. showed that coexpression of AKT and N-Ras using hydrodynamic transfection resulted in a dramatic acceleration in liver cancer development[88]. This group also demonstrated the *in vivo* crosstalk between the AKT and Ras pathways in promoting liver tumor development, and the pivotal role of mTORC1-dependent and independent pathways in mediating AKT and Ras induced hepatocarcinogenesis. Ras induced hepatocarcinogenesis[88]. Stauffer et al. showed that the coactivation of AKT and β-catenin (AKT/CAT) in hepatocytes can generate the development of a lipogenic tumor phenotype[89].

ICC is another major type of liver cancer, but there are only a few available mouse models for ICC. Subcutaneous xenograft models of ICC have been developed but data derived from these xenograft systems correlate poorly with the clinical outcome[67, 90-93]. Recently, Fan et al. generated a new ICC mouse model by overexpressing intracellular domain of Notch1 receptor (NICD1) or by co-expressing activated AKT and Notch (AKT/NICD) into the mouse liver[94]. NICD1 alone is sufficient to promote ICC development, however only after 20 to 25 weeks of latency[95]. Importantly, ICC formation was significantly accelerated by co-expression of activated AKT and NICD, leading to a fully developed stage around 5 weeks after injection[94].

Chapter 2

A novel system for in vivo imaging of free fatty acid uptake in the liver

Significance and background

In obesity, plasma levels of free fatty acids (FFA) are usually elevated and are associated with an increased risk of hepatosteatosis, the hallmark feature of nonalcoholic fatty liver disease (NAFLD)[96]. FFA-induced liver dysfunction contributes to dyslipidemia and eventually leads to the development of type 2 diabetes[97]. Some deleterious effects of excessive FFAs on liver function can be prevented by inhibiting fatty acid transport proteins(FATPs) in the liver, thereby reducing FFA hepatic uptake[98]. Glitazones, a class of drugs used in the treatment of diabetes mellitus type 2, have been shown to prevent hepatosteatosis and exert anti-diabetic effects by clearing FFAs present in the circulation[99, 100]. Thus, quantitative monitoring of long-term hepatic FFA uptake in vivo should be of paramount importance for lipid research and the liver-associated metabolic disorders.

While several imaging technologies have been developed for spatiotemporal imaging of FFA flux in living animals, they suffer shortcomings that limit their use in research settings. For example, positron emission tomography (PET) has been used to examine cardiac fatty acid metabolism, but 11C-palmitate, the main FFA probe for PET, has a very short half-life and requires an onsite cyclotron, making this technique unsuitable for most laboratory settings[101]. The validity of another FFA PET probe used in metabolic studies, 14-(R,S)-(18)F-fluoro-6-thiaheptadecanoic acid ((18)F-FTHA), as a mimic of natural fatty acid uptake, has recently been called into question as it fails to detect the reduction of β-oxidation under hypoxic conditions[102]. Single Photon Emission Computed Tomography (SPECT) for small animals has been increasingly used to study myocardial metabolism in heart disease; however, SPECT suffers from technical limitations including relatively poor temporal and spatial resolution, and the inability to differentiate circulating from intracellular fatty acids[103]. In addition to technical limitations, PET and SPECT are costly and require specialized instrumentation.

These challenges prompted us to pursue bioluminescence imaging (BLI) of FFA fluxes using a sensitive readily available charge-coupled device (CCD) camera as a detector. We recently developed a BLI probe for monitoring FFA uptake (FFA-Luc)[42]. FFA-Luc is a long-chain fatty acid linked to luciferin with a disulfide bond (Fig 2.1). Cellular uptake exposes the probe to the reducing intracellular environment resulting in cleavage of the disulfide bond and the uncaging of luciferin. Thus, in luciferase expressing cells FFA-Luc uptake results in the proportional generation of photons[42]. We showed that FFA-Luc influx occurred via a physiological transport process similar to that for natural FFAs and

could be monitored in live animals in real time using BLI. Using mice that express luciferase under the actin promoter (FVB-Luc+), we could detect FFA uptake from the intestine and distinct sites such as brown adipose tissue. However, we were not able to unequivocally determine hepatic fatty acid uptake due to the high scattering of multiple signals from the abdominal cavity. To address this problem, we generated transgenic mice with liver-specific expression of luciferase (L-Luc mice).

Here, we show that our in vivo model based on the application of the FA-SS-Luc probe in L-Luc mice is a powerful tool to quantitatively assess FA hepatic uptake in real-time settings and to reveal dynamic metabolic changes triggered by different physiological conditions.

Results and discussion

The FFA-luc system was developed in collaboration with the laboratories of Drs. Dubikovskaya and Bertozzi at UCB. All FFA-luc compounds utilized here were provided by Dr. Dubikovskaya, EPFL.

Generation of liver-specific transgenic mice

The L-Luc mouse model was generated by crossing mice bearing the Gt(ROSA)26Sor$^{tm1(Luc)Kael}$ allele with Tg(Alb-cre)21Mgn mice. As a result, the offspring expressed luciferase under the control of the albumin promoter. To test this model, we injected luciferin intraperitoneally into FVB-Luc$^+$ mice and L-Luc mice. While FVB-Luc$^+$ mice showed signal throughout the body, the signal from L-Luc mice was liver specific (Fig 2.2A). To further confirm liver-specific luciferase expression, we harvested several organs and detected light emission only in the liver (Fig 2.2B). The dose-response in L-Luc mice was investigated by injecting 2, 10, and 20mM of luciferin and 10, 50, and 100µM of FFA-Luc, followed by determining total photon flux for each animal by drawing a region of interest around the apparent liver and integrating the photon flux over the total imaging period. The results indicated a dose-dependent increase in total photon flux after both luciferin and FFA-Luc injection (Fig 2.3A, B).
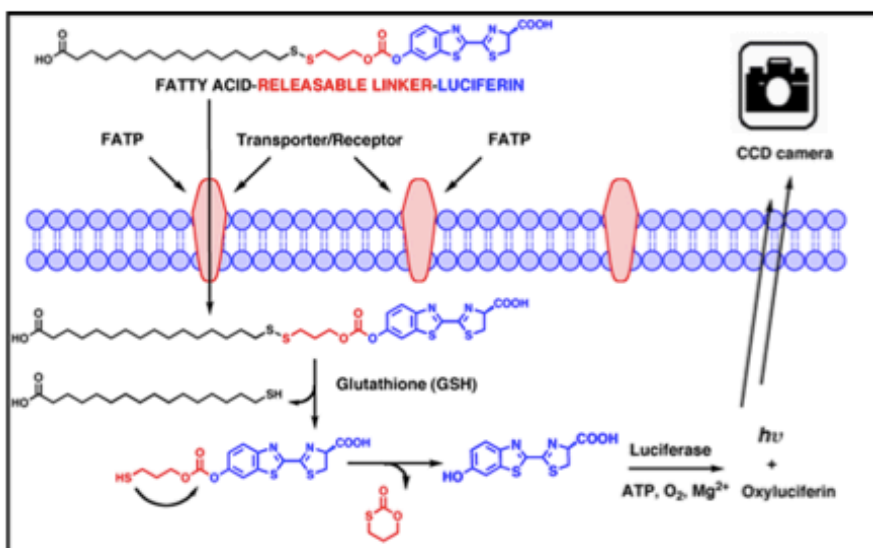
Figure 2.1. Scheme of fatty acid probe (FFA-Luc) for BLI.
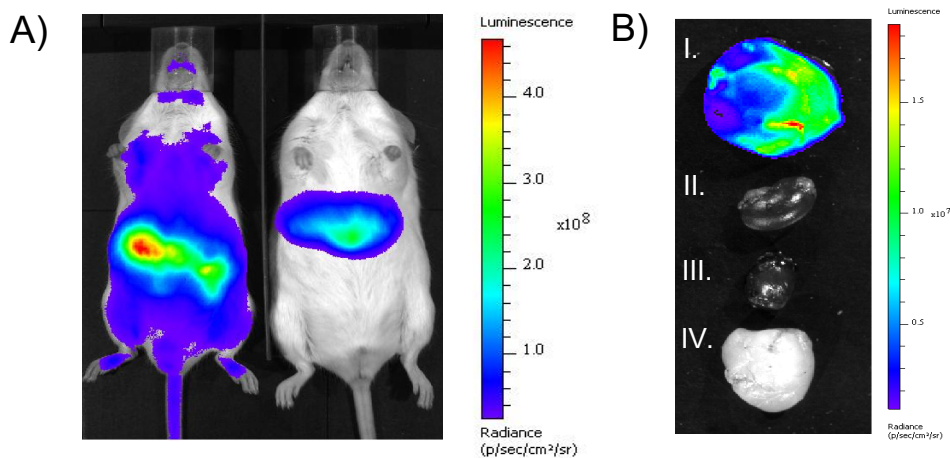
Figure 2.2. Generation transgenic mice and model validation
A) Overlay of ventral luminescence and black/white images of FVB-Luc+(left) and
L-Luc (right) mice 5 min after intraperitoneal injection of 100μL luciferin (2 mM
solution in PBS).
B) Overlay of luminescence and black/white images of the liver (I), kidney (II),
heart (III), and white adipose tissue (IV) from L-Luc mice 5 min after luciferin
administration.

Evaluation of fatty acid-luciferin probe in L-Luc mice

As the probe is taken up by all FFA utilizing tissues with subsequent generation of luciferin regardless of luciferase expression[42], we considered the possibility that luciferin uncaged in extrahepatic tissues could circulate back to the liver and thus contribute to the hepatic BLI signal independent of hepatic FFA uptake. To determine serum levels of FFA-Luc-derived free luciferin, we measured luciferin content in serum samples of FFA-Luc- and luciferin-injected wild-type mice 10 and 20 min post FFA-Luc injection by a luminometer using exogenous luciferase and ATP (Fig 2.4A). Based on the serum luminescence data and a standard curve based on known luciferin concentrations, we calculated a serum free luciferin concentration of 0.16µM 20 min post FFA-Luc injection. Through a series of in vivo injection experiments we determined further that this serum concentration of luciferin can also be achieved using a single 100µL IP injection of 4µM free luciferin. We injected this dose into the L-Luc mice to determine the signal intensity in the liver generated by free circulating luciferin at a concentration expected to be reached by extrahepatically generated breakdown of the FFA-Luc probe (Fig 2.4B). The results indicate that the maximal total signal generated by 0.16µM circulating luciferin (emulating luciferin uncaged outside the liver) was less than 4% of the total signal we observe for FFA-Luc, and thus within the range of inter-animal variations. Cumulatively, these findings demonstrate that the luminescence detected after FFA-Luc injection into L-Luc mice predominantly reflects hepatic FFA uptake.
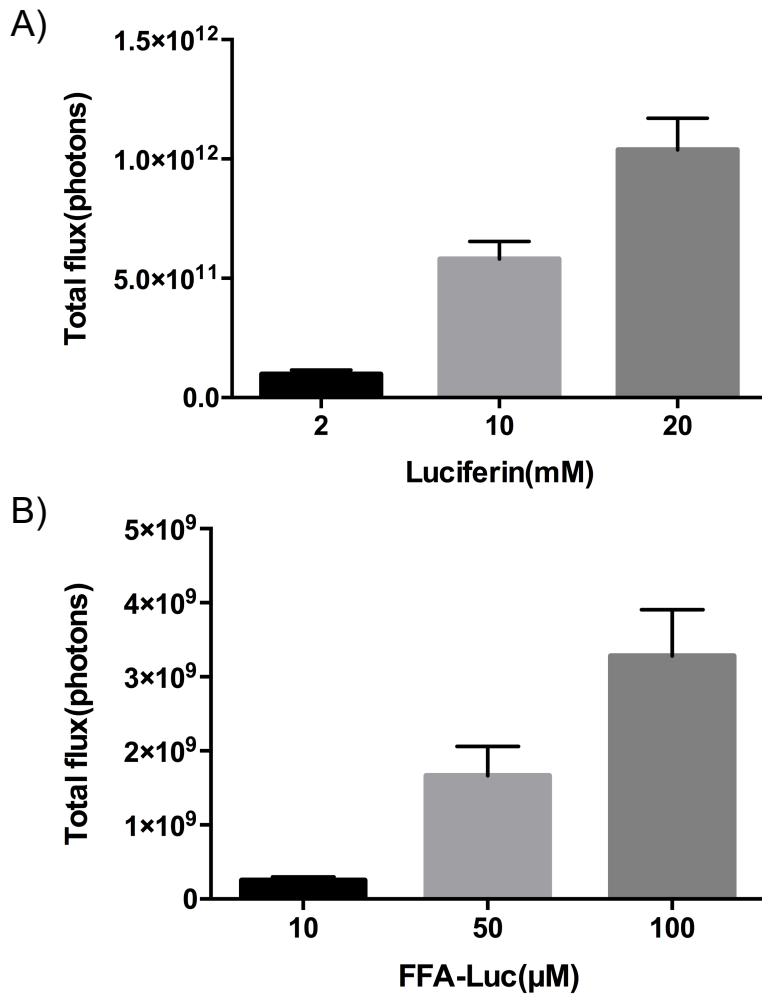
Figure 2.3. Dose dependent response to luciferin and FFA-luc in L-Luc mice
A) Total luminescence over 25 min resulting from bioluminescent signal after IP injection of luciferin (100µL of 2mM solution in PBS). Error bars are ± SD (n=5).
B) Total luminescence over 50 min resulting from bioluminescent signal after IP injection of FFA-Luc (100µL of 200µM solution bound to 0.1% BSA in PBS). Error bars are ± SD (n=5).
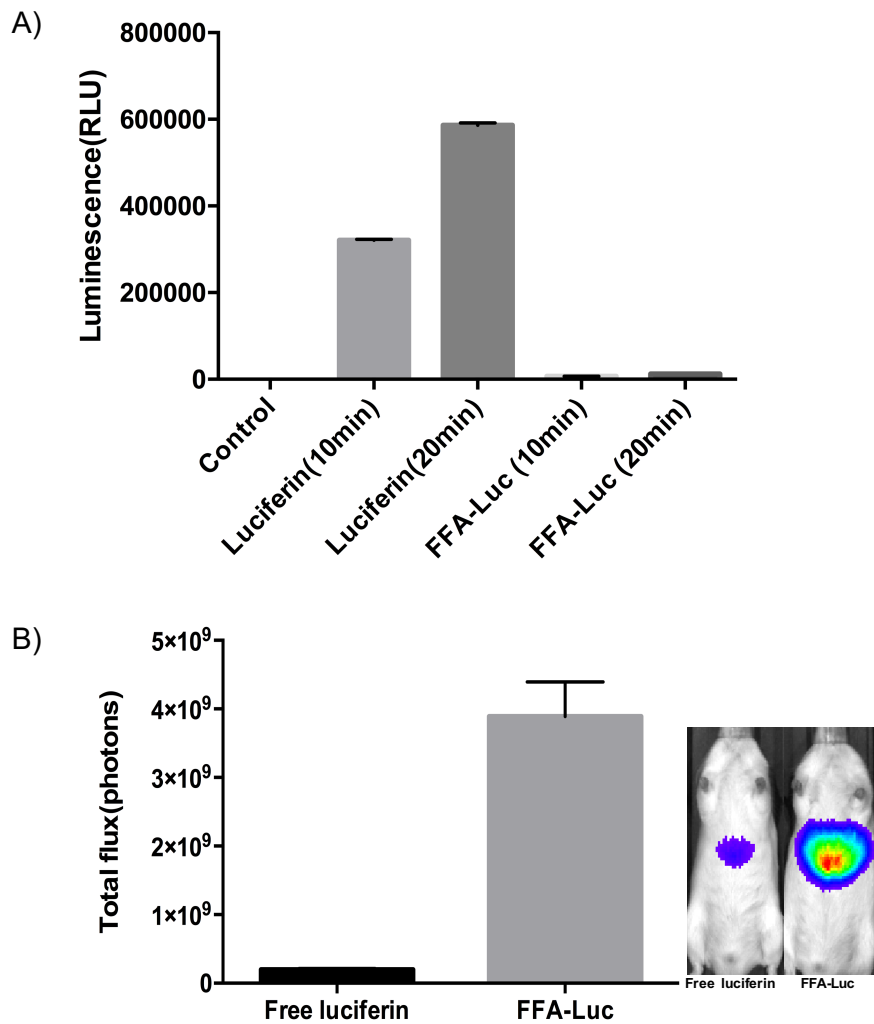
Figure 2.4. Measurement of the circulating free luciferin
A) Detection of free serum luciferin before injection, 10 and 20 min after the injection of luciferin and FFA-Luc. Error bars are ± SD (n=4).
B) Luminescence emitted by free luciferin injected at a dose (100μL at 4μM) to match the serum levels of FFA-derived circulating free luciferin (0.16μM in serum). Error bars are ± SD (n=4).

Applications of BLI analysis of FA hepatic uptake in different physiological conditions

Next, we determined whether our imaging system for the in vivo detection of hepatic FFA uptake can be used to detect changes in liver FFA uptake. Our previous study showed that natural secondary bile acid, deoxycholic acid (DCA), suppresses hepatic FFA uptake through inhibition of a specific fatty acid transporter, FATP5[104]. To compare our novel in vivo assay to a widely used method for ex vivo measurement of FFA uptake we measured FFA influx in the liver of DCA-treated L-luc mice using BLI with FFA-Luc and compared the measurement to an endpoint assay with fluorescently labeled FA (BODIPY) (Fig 2.5A,B). While only the bioluminescent method allowed for in vivo detection, both FFA-Luc and BODIPY-FFA based assays detected a comparable decrease in hepatic FFA uptake of 35% in the DCA-treated group. This finding suggests that our BLI system could successfully replace an end-point FFA uptake assay requiring animal euthanasia and enables in vivo monitoring of the changes in FFA uptake under physiological or pathological conditions.

We then applied our imaging approach to the detection of novel phenomena. A previous study had shown that fenofibrate, a pharmacological PPARα agonist used to reduce cholesterol levels, promotes β-oxidation and lipogenesis in the liver[105]. However, the effects of fenofibrate on FFA hepatic uptake have not yet been explored. Therefore, we tested whether BLI could be applied for this purpose. L-Luc mice were fed standard chow or fenofibrate (0.2% w/w) supplemented diet for 10 days and then analyzed for FFA uptake in the liver. The results revealed a significant increase by 40% of hepatic FFA uptake in fenofibrate-treated animals compared to control (Fig 2.6), suggesting that enhanced FFA uptake contributes to the fenofibrate-induced increase in β-oxidation. To the best of our knowledge, these are the first data showing the effect of fenofibrate on FFA uptake in the liver.
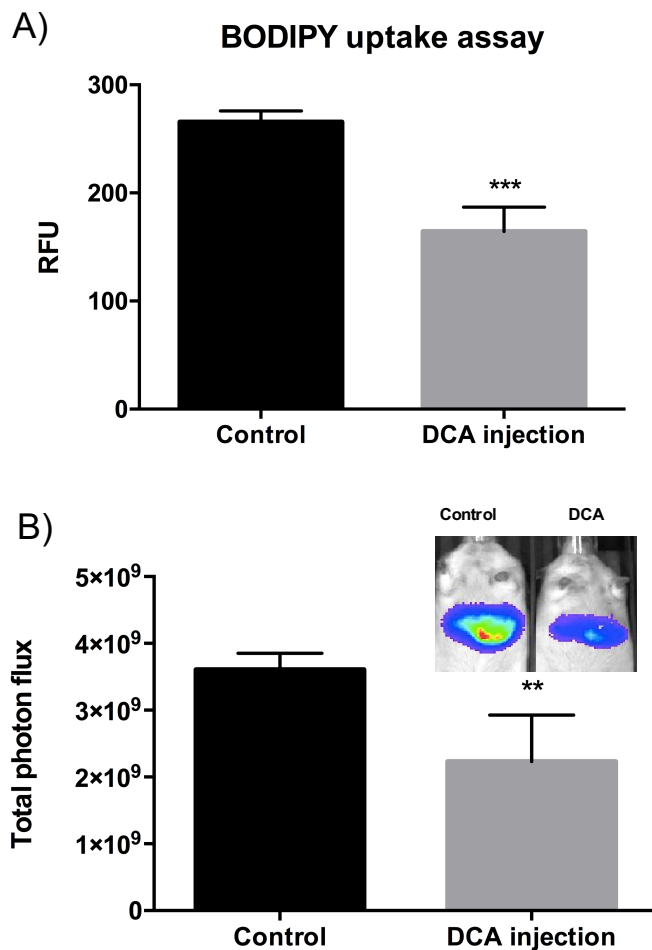
Figure 2.5. Detection of hepatic FFA uptake inhibition by DCA treatment
A) Acute effects of deoxycholic acid (DCA) injected at the concentration of 6.4 mg/kg body weight into L-Luc mice on the reduction of hepatic uptake of a fluorescence-labeled fatty acid (BODIPY). Statistical analyses were performed with a Student's t-test. **P < 0.01 (n = 4), and error bars are ± SEM.
B) Acute effects of DCA on the reduction of FFA-Luc hepatic uptake. Total photon uptake was determined for 50 min post-injection. The inset demonstrates the overlay of mouse ventral luminescence and black/white images 20 min after IP injection of DCA and FFA-Luc. Statistical analyses were performed with a Student's t-test. **P < 0.01 (n = 4), and error bars are ± SEM.
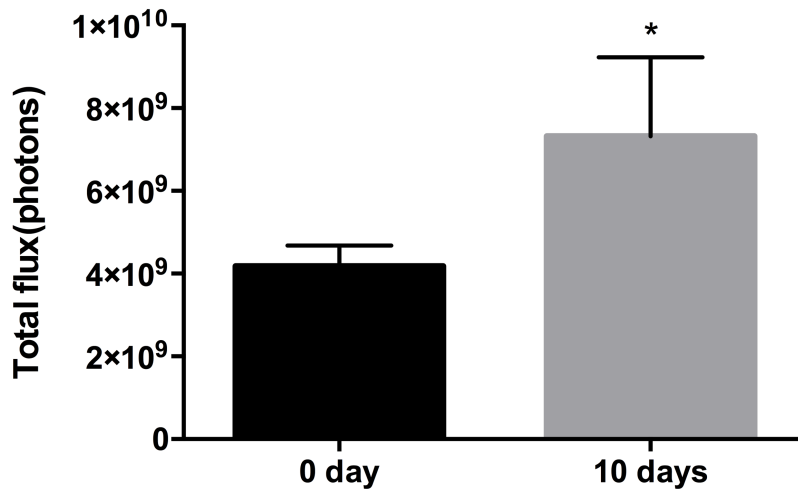
Figure 2.6. Detection of hepatic FFA uptake increase after fenofibrate feeding.
Acute effects of fenofibrate on the reduction of FFA-Luc hepatic uptake. Total photon uptake was determined for 50 min post-injection. Statistical analyses were performed with a Student's t-test. *P < 0.05 (n = 5), and error bars are ± SEM.

Diurnal rhythm of hepatic fatty acid uptake

As our imaging approach is well suited for longitudinal studies, we next explored hepatic diurnal changes in liver FFA uptake. The diurnal clock plays an important role in the regulation of plasma and tissue levels of lipids, including triglycerides, cholesterol, and FFAs[106, 107]; however, the effects of diurnal rhythms on hepatic FFA uptake have not been thoroughly investigated, in part due to the lack of non-invasive methods that could be used in live animals. Therefore, we applied BLI to analyze the dynamics of FFA hepatic uptake over a 24-hour period in male L-Luc mice. The first injection of FFA-Luc was conducted at zeitgeber time (ZT; lights off at ZT12) 06 (1 PM) followed by subsequent injections every 30 hour, and the signal was measured every time for 20 min. The highest FFA uptake was observed at ZT06, mid-light phase, while the lowest was detected at ZT18 (Fig 2.7A); moreover, significant differences were observed between ZT06 and ZT12 (decreased by 59% of ZT06) and between ZT06 and ZT18 (decreased by 64% of the highest). These results indicate that FFA uptake by the liver is altered across the day and night, suggesting a robust diurnal rhythm. These data agree with the finding that FATP2, one of the major hepatic fatty acid transporters, exhibits a strong diurnal expression pattern[108]. Importantly the rhythmic changes in hepatic FFA uptake were not driven by changes in circulation FFA levels, and resulting differences in specific activity of the probe,

as shown by the different daily profile of circulating FFA levels relative to that of hepatic FFA uptake (Fig 2.7B). These results further underscore the utility of our system for quantitatively monitoring changes in hepatic FFA levels independent of changes in circulating FFAs and the ability to detect a liver-specific phenomenon in the organisms over time.
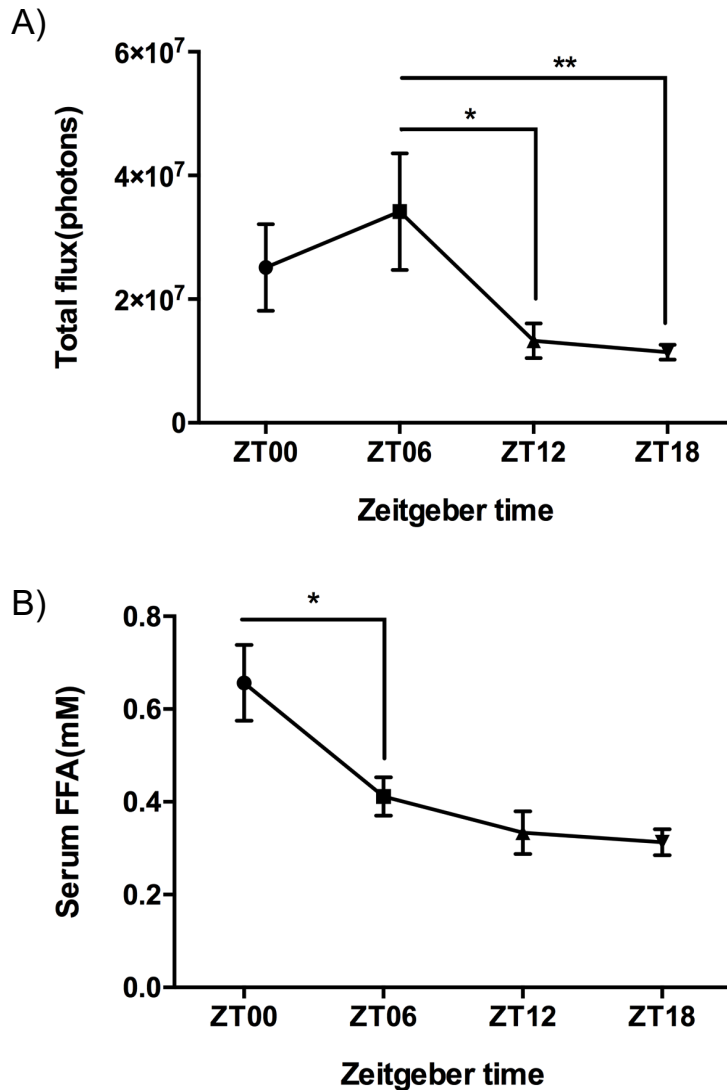
Figure 2.7. Diurnal regulation of hepatic FFA uptake
A) FFA uptake rate after the injection of FFA-Luc into L-Luc mice during the light (ZT6, ZT12) and dark (ZT18, ZT0) periods. Statistical analyses were performed with a two-tailed Student's t-test. **P<0.05***P < 0.01 (n = 5), and error bars are ± SEM.

B) Serum was collected at the same time points as in A) and FFA concentration was measured. Statistical analyses were performed with a two-tailed Student's t-test. *P < 0.05 (n = 5), and error bars are ± SEM.

Conclusion

Taken together, we have demonstrated the development of a novel in vivo imaging system and its application for monitoring physiological and pathological changes in hepatic FFA uptake in preclinical models. The application of a bioluminescent FFA probe in L-Luc transgenic mice enables real-time detection and analysis of FFA uptake specifically in the livers of these models. Our results establish this system is a useful tool to investigate metabolic changes induced by pharmacological agents and uncover novel and unexpected regulatory factors such as diurnal rhythm of hepatic FFA uptake in longitudinal studies. The data obtained in this study demonstrate that FFA uptake could be monitored in real time under various conditions, which, given the importance of FFA hepatic accumulation in physiology, opens up a spectrum of opportunities for studying fundamental mechanisms underlying lipid metabolism in the liver.

Chapter 3

The role of fatty acid transport proteins FATP2 and FATP5 in intrahepatic cholangiocarcinoma

Significance and background

Intrahepatic cholangiocarcinoma(ICC) is a relatively rare form of liver cancer; however, its incidence and mortality are increasing worldwide[49, 109]. In the United States, the age-adjusted incidence of ICC increased from 0.32 per 100,000 population in 1975 to 0.95 per 100 000 population in 2015[49, 50]. Although this increased of incidence is attributed to advances in diagnostic technologies that allow early-stage detection of ICC[110], recent studies have additionally implicated risk factors such as viral hepatitis, diabetes mellitus and fatty liver disease[111, 112]. Currently, there is no FDA-approved targeted therapy for ICC; therefore, treatment for this primary liver cancer remains a significant unmet medical need.

There is increasing evidence that tumor cells require "metabolic reprogramming", which involves changes in cellular bioenergetics that result in malignant transformation and tumor development[113]. Cancer cells have been shown to utilize adaptive metabolic pathways to sustain their viability even in the absence of extracellular nutrients[113]. For instance, cancer cells show specific alterations in lipid metabolism; de novo lipogenesis is often up-regulated in numerous types of cancers. Further, tumor cells in general are less dependent on exogenous free fatty acids (FFAs) for growth[114, 115]. Increased expression and activity of fatty acid synthase (FASN), the central enzyme involved in de novo lipogenesis, is required for the survival and proliferation of many tumor cells and has been considered a potential therapeutic target in cancer[116-118]. As most studies of lipid metabolism in cancer have focused on de novo lipogenesis, the role of exogenous fatty acids has been largely ignored. However, FASN inhibitors are only capable of inhibiting cell growth in the absence of exogenous fatty acid sources[119]. Obesity, which is associated with elevated circulating fatty acid levels, has been implicated as a major risk factors for the development of multiple tumor types[120, 121]. Furthermore, a recent study demonstrated that FASN dependence is not a universal feature in liver cancer, as ICC development is insensitive to FASN deprivation; however, the development of hepatocellular carcinoma (HCC) is highly dependent on FASN[122]. These findings support the role of exogenous fatty acids in the development of cancers, particularly ICC.

The protein-mediated transport of FFAs, which occurs in numerous physiological and cellular processes, has been proposed as the major mechanism underlying the uptake of long chain fatty acids (LCFAs)[123]. Fatty acid transport proteins (FATPs) are major transmembrane proteins that participate in LCFA uptake; among these, FATP2 and FATP5 are robustly expressed in the

liver[124]. In order to investigate the role of FATPs in the liver, we generated both genetic knockout models[125] and adeno-associated virus-based knockdown models[126, 127]. Using these theses animal models we demonstrated that the inhibition of FATP2 and FATP5 reverses already established fatty liver disease and prevents the deleterious effects of excessive FAs on the liver[127, 128]. In addition, we recently developed a bioluminescence-based FFA imaging probe (FFA-Luc) to enable quantitative monitoring of long-term hepatic FFA uptake in live animals[42].

However, to date, this technology has not been applied to address the hypothesis that FATPs mediated uptake of exogenous FFAs plays pivotal role in the development of ICC. To test the hypothesis, we generated a murine ICC model by overexpressing the activated forms of AKT and intracellular domain of Notch receptor (AKT/NICD) with hydrodynamic transfection[94] and applied our previously developed novel technology to this animal model. The present study uncovered the critical role of FATP5 and aberrant FFA metabolism during ICC development and demonstrated the potential utility of these proteins as therapeutic targets for the prevention and treatment of ICC.

Results and discussion
The ICC and HCC model systems used in this study were adapted from our collaborator Dr. Chen at UCSF and FFA-luc was provided by our collaborator Dr. Dubikovskaya at EPFL.

Construction and validation of a reporter for monitoring of tumor formation
In order to monitor tumor formation in vivo, we generated a reporter construct expressing AKT and firefly luciferase under a single promoter. A reporter vector was constructed based on the vector backbone pT3-EF1α (gifted by Xin Chen). IRES-Luciferase was amplified from MSCV-IRES-Luciferase plasmid (Addgene; #18760) by PCR, using primers with EcoRI recognition sequences. PCR products were purified and cloned into the pT3-EF1α vector and the reporter vector was named AKT-Luc (Fig 3.1A).

Previous studies have shown that co-expression of activated forms of AKT and Ras (referred to herein as AKT/Ras) and AKT/NICD in the mouse liver significantly accelerates the development of HCC and ICC, respectively[88, 94]. We firstly injected AKT-Luc alone or with/without additional plasmid, NICD, or Ras to test whether AKT-Luc/Ras and AKT-Luc/NICD, like the original vector, induce tumor formation. We performed hydrodynamic injection in 7-week-old male FVB mice and extracted livers 8 weeks after injection. As shown in Fig 3.1B, both AKT-Luc/Ras and AKT-Luc/NICD successfully induced the formation of tumors in the mouse livers.

A)

pT3-EF1α-GeneX — IR — EF1α — AKT IRES Luciferase — Poly(A) — IR

pT3-EF1α-GeneX — IR — EF1α — NICD — Poly(A) — IR

pT3-EF1α-GeneX — IR — EF1α — Ras — Poly(A) — IR

pCMV-SB — CMV — SB Transposase

B)

| AKT/NICD | AKT-Luc/NICD | AKT-Luc/Ras |
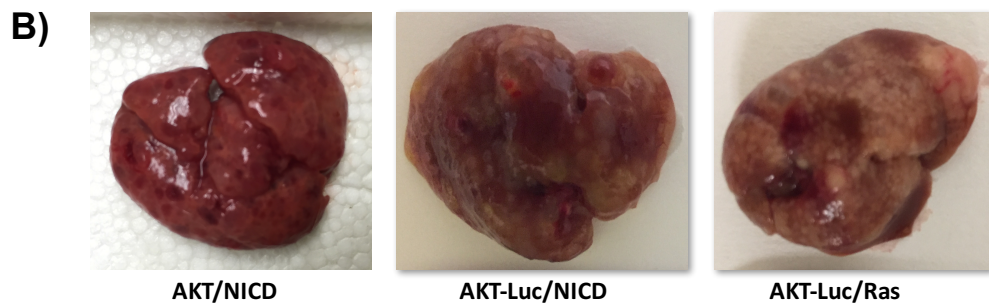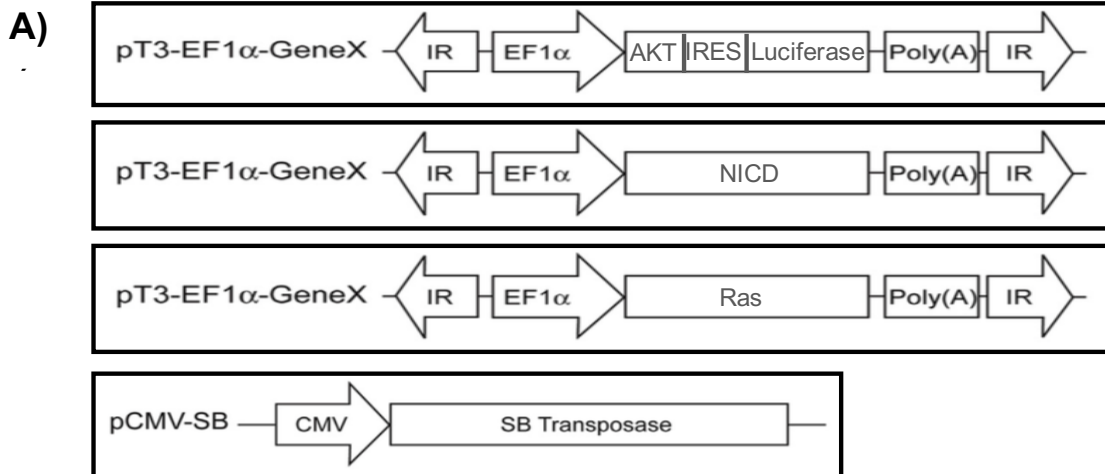
Figure. 3.1. AKT-Luc/Ras and AKT-Luc/NICD induced HCC and ICC formation
A) Structures of constructs used in the study
B) Photographic images of mouse livers taken at 7 weeks following the hydrodynamic injection of corresponding plasmids

In order to investigate whether the bioluminescence signal indicates tumor growth, we first performed hydrodynamic injection and bioluminescence imaging (BLI) to monitor the establishment and growth of liver tumors starting at 7 days post-injection. One group received AKT-Luc/Ras and the other received AKT-Luc/NICD. Each group of mice received weekly intraperitoneal injections of D-luciferin, and the bioluminescence signal was measured using IVIS Spectrum (Caliper Life Sciences). Total photon flux (photons/second) of regions of interest were calculated with the IVIS Living Image software. The bioluminescence within the liver in both groups was observed to increase with time (Fig 3.2). After 7 weeks, mice were sacrificed and examined for tumor development; tumors were detected in the livers of both groups. Importantly, bioluminescence was only detected in tumor nodules, indicating a positive correlation between bioluminescence intensity prior to liver tumor extraction in vivo and tumor growth (Fig 3.2). These studies validate the use of AKT-Luc plasmids and BLI to monitor liver tumor growth *in vivo.*

Following the injection of the plasmids, the bioluminescence signal was stable for HCC but decreased for ICC up to 3 weeks; then, an increase in the signal was observed (Fig 3.2). This trend is consistent with previous results in that while up to 40% of the hepatocytes may receive the injected plasmids, only 2% to 5% undergo long-term integration by the Sleeping Beauty (SB) transposase mediated somatic integration. The unintegrated plasmid emits a signal for about 1 week, and is then degraded[82, 129].
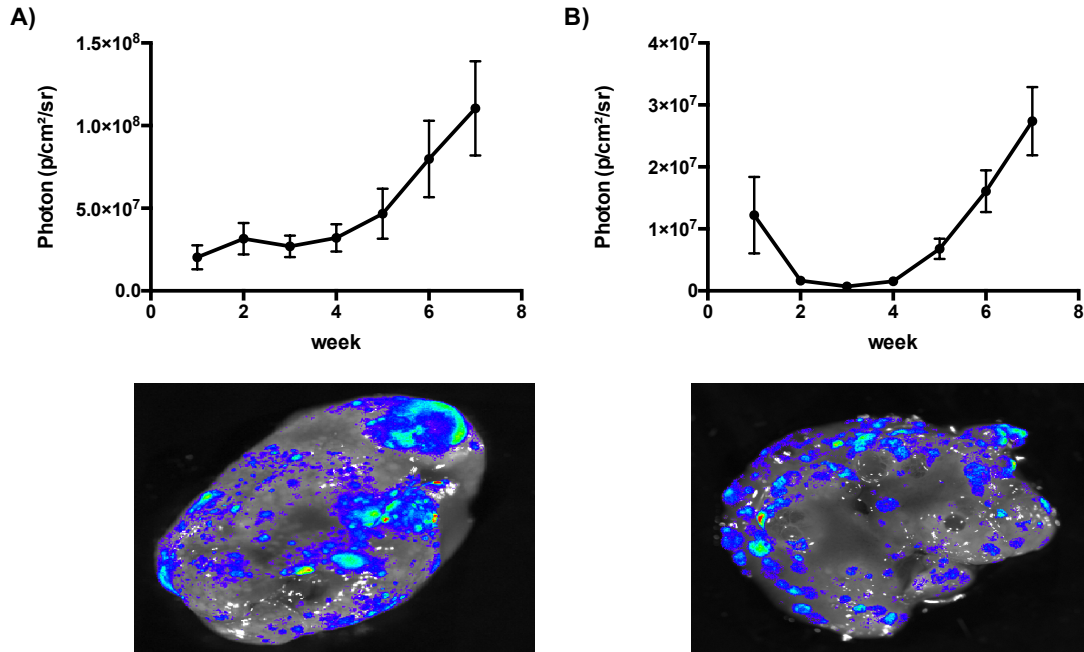
Figure. 3.2. Bioluminescence imaging of tumor growth
A) Bioluminescence signal from AKT-Luc/Ras was measured every week after hydrodynamic injection; photographic images of mouse livers taken at 7 weeks after D-luciferin injection. Error bars are ± SD (n=3).
B) Bioluminescence signal from AKT-Luc/NICD was measured every week after hydrodynamic injection; photographic images of mouse livers taken at 7 weeks after D-luciferin injection. Error bars are ± SD (n=3).

Differences in the kinetics of fatty acid uptake between HCC and ICC

To investigated the differences in the utilization of exogenous FAs between HCC and ICC, we first measured and compared FFA uptake in HCC and ICC using BLI with FFA-Luc (Fig 3.3); 7 weeks after hydrodynamic injection, mice were injected with FFA-Luc. Photon flux was monitored over the total imaging period. Total flux reflecting FFA uptake was determined by drawing a region of interest around the apparent liver and integrating the photon flux for 50 minutes. Interestingly, a statistically significant decrease in FFA-Luc signal normalized to D-luciferin signal was observed in the HCC mice, indicating that the livers of mice with HCC take up a lower amount of FFA than ICC those of mice (Fig 3.3A).

In order to confirm this finding, primary tumor cells were isolated from mice following the development of tumors (7 weeks after the injection of oncogenes). Additionally, wild-type primary hepatocytes were isolated and FFA uptake in each group was compared using fluorescently (BODIPY) labeled fatty acids. Primary cells were isolated with BODIPY for 5 minutes and total cell numbers showing fluorescence were counted by flow cytometry. Total cell numbers of the HCC group that showed fluorescence were significantly smaller than those of the ICC group (20%), implying that the uptake of FFA rate is significantly higher in ICC primary cells than in HCC primary cells (Fig 3.3B).

FFA uptake was found to differ between ICC and HCC; therefore, we examined the changes in the expression of genes involved in hepatic fatty acid uptake. We have previously shown that FATP2 and FATP5 play a key role in hepatic fatty acid uptake[128, 130]. Therefore, we investigated mRNA expression levels of FATP2 and FATP5 via qPCR analysis (Fig 3.4). The mRNA levels of genes encoding FATP2 were found to have decreased by 83% in the livers of mice with HCC relative to the livers of wild-type mice; however, a decrease of only 40% was observed in the livers of mice with ICC relative to the wild type. The FATP5 mRNA level decreased by 85% in mice with HCC but ~30% in those with ICC, relative to the wild type (Fig 3.4).

The present results demonstrated that the rate of FFA uptake decreases significantly during the development of HCC, but not ICC. These data are consistent with gene analysis results, showing that the expression of FATP2 and FATP5, which are responsible for hepatic FA uptake, decreases during ICC. These findings may be attributable to the fact that ICC is not dependent on FASN[122]. FATP2 and FATP5 are expressed at the wild-type level in ICC, suggesting that the availability of fatty acids is sufficient; as such, the de novo synthesis of fatty acids is not required.
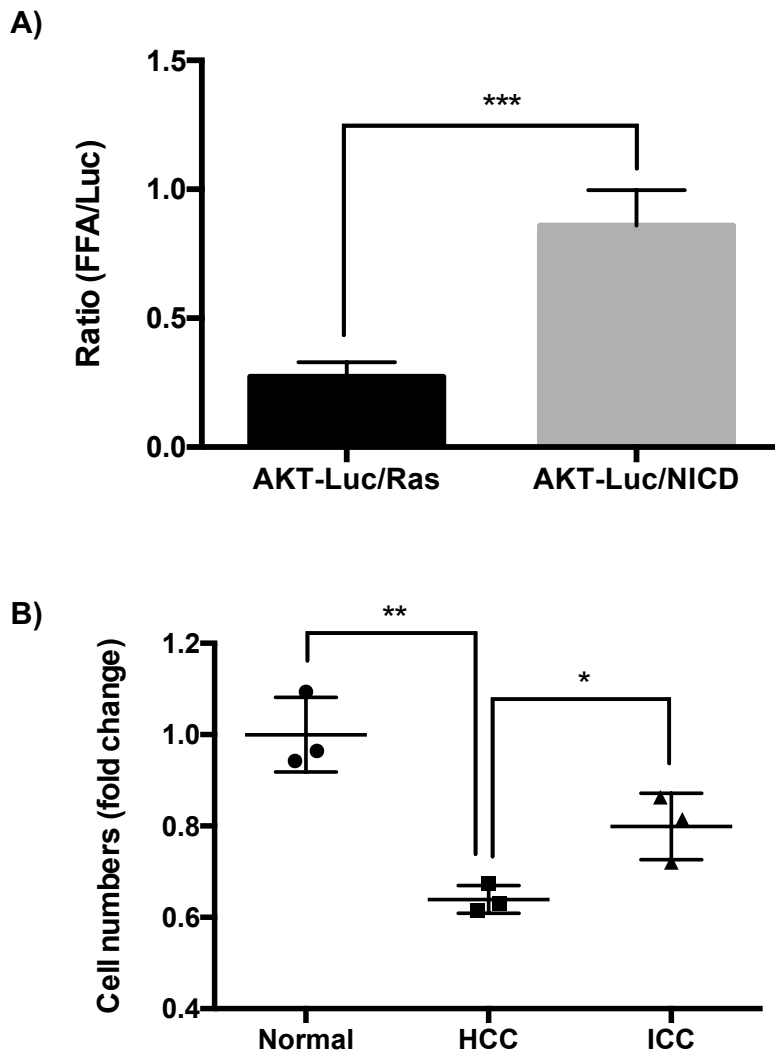
Figure. 3.3. LCFA uptake differences between HCC and ICC
A) FFA-Luc hepatic uptake at 7 weeks; total photon uptake was determined for
50 min post-injection. Statistical analyses were performed with a Student's t-test.
***$P < 0.001$ (n = 5), and error bars are ± SEM.
B) Uptake of a fluorescence-labeled fatty acid (BODIPY) in primary cells
Statistical analyses were performed with a two tailed Student's t-test. *$P < 0.05$,
**$P<0.01$ (n = 4), and error bars are ± SEM.
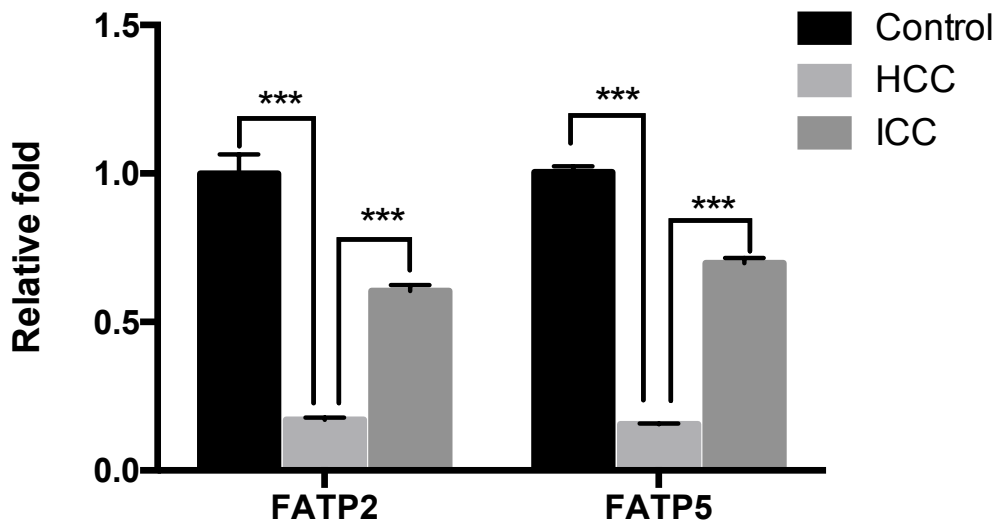
Figure. 3.4. Gene expression of FATP2 and FATP5 in HCC and ICC
qPCR was performed on cDNA synthesized from isolated RNA of each type of tumor (HCC and ICC) to determine mRNA expression levels of *FATP2* and *FATP5*. Statistical analyses were performed with a two tailed Student's t-test. ***$P<0.001$ (n = 4), and error bars are ± SEM.

Suppression of tumor formation in ICC via inhibition of *FATP5* expression

The present findings indicate that FATP2 and FATP5 are expressed at normal levels in ICC; therefore, FFA uptake in the liver is not affected in this form of cancer. We examined whether loss of FATPs affects tumor formation. In a previous study, we generated FATP2 and FATP5 shRNA expression constructs, as well as a scramble(SCR) shRNA with no complementarities to any known gene sequence in the mouse genome. The RNA interference effect of the latter was confirmed[127, 128]. For in vivo studies, we used adeno-associated vectors to package and express FATP2, FATP5, and SCR shRNA, and demonstrated that the expression of FATP2 and FATP5 were considerably blunted (>95% inhibition) in adeno-associated vector-injected mice.

First, we tested the effect of loss of FATP5 on HCC and ICC development. FVB male mice were injected via the tail vein with the adeno-associated vector; then, hydrodynamic injection was administered 10 days later. Bioluminescence signal was measured weekly after hydrodynamic injection and total photon flux (photons/second) of regions of the liver were calculated. In the AKT-Luc/Ras

injection group, signal from mice with adeno-associated vector SCR exhibited an increase for 9 weeks (Fig 3.5A); however, the signal from the adeno-associated vector FATP5 group decreased gradually (Fig 3.5B). At 9 weeks following the injection of plasmids, mice were sacrificed. Tumor formation was detected in the adeno-associated vector SCR groups but not in the adeno-associated vector FATP5 groups.

In order to confirm the effects of FATP5 on tumor formation, we monitored tumor growth in FATP5 knockout (KO) mice; AKT-Luc/Ras and AKT-Luc/NICD were injected into C57 and FATP5 KO mice. The bioluminescence signal was measured weekly; following the injection of AKT-Luc/NICD, an increased signal was detected in C57 mice, but not in FATP5 KO mice (Fig 3.6B). However, tumor suppression was not detected in FATP5 KO mice following the injection of AKT-Luc/Ras (Fig 3.6A). Both C57 and FATP5 KO mice were found to develop HCC following AKT-Luc/Ras injection.

Since we couldn't detect HCC tumor suppression in the FATP5 KO mouse and ICC showed robust hepatic FFA uptake than HCC (Fig 3.3), we decided to further investigated effects of loss of FATP5 function on ICC growth. In order to test whether FATP5 knockdown delays ICC formation growth after the onset of the tumor, we injected adeno-associated vector FATP2 and FATP5 after hydrodynamic injection. Mice were first administered hydrodynamic injections; two weeks later, adeno-associated vectors were administered. Interestingly, no delay in tumor growth was observed in the mice receiving injections of SCR and FATP2; however, the FATP5 group showed significant reduction in tumors at 7 weeks (Fig 3.7).
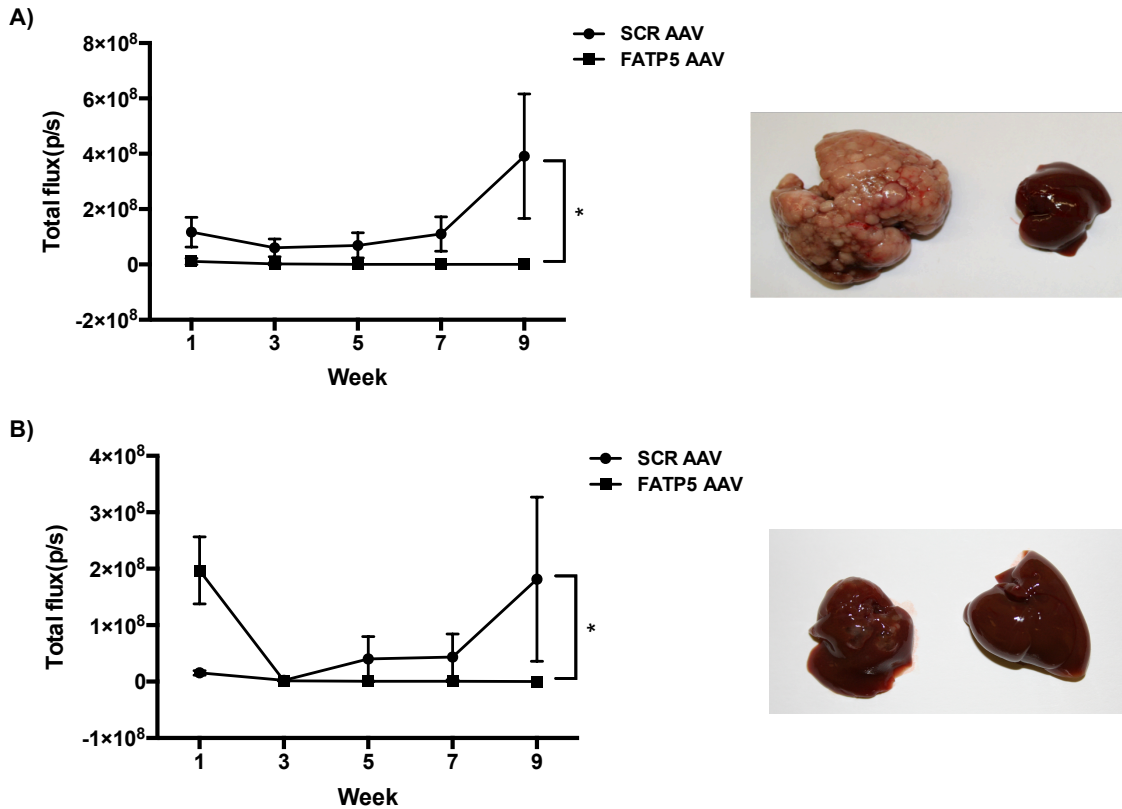
Figure. 3.5. FATP5 knockdown using adeno-associated virus suppressed tumor development

A) AKT-Luc/Ras injection; bioluminescence was measured every week. Livers were extracted after BLI for 9 weeks. Statistical analyses were performed with multiple Student's t-test. *$P < 0.05$ (n = 4), and error bars are ± SEM.

B) AKT-Luc/NICD; Bioluminescence was measured every week. Livers were extracted after BLI for 9 weeks. Statistical analyses were performed with multiple Student's t-test. *$P < 0.05$, **$P < 0.01$ (n = 4), and error bars are ± SEM.
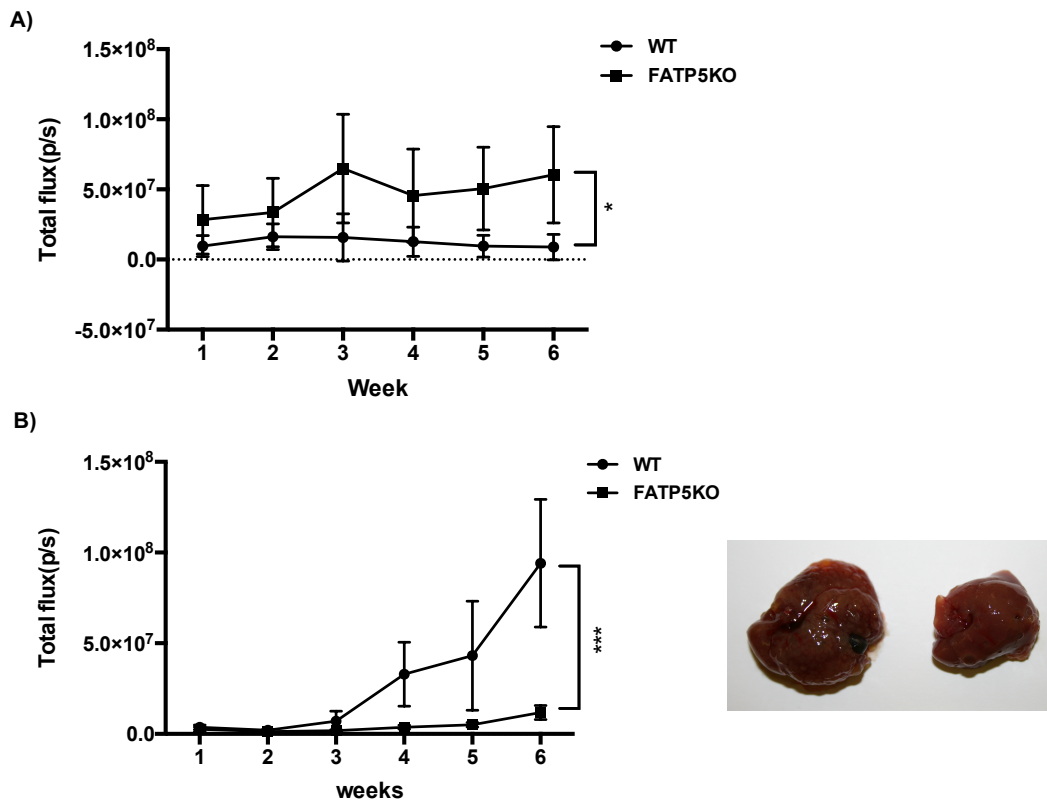
Figure. 3.6. Suppression of ICC tumor formation in FATP5 KO mice
(A) AKT-Luc/Ras injection; bioluminescence was measured every week.
Statistical analyses were performed with multiple Student's t-test. *P < 0.05 (n =
5), and error bars are ± SEM.
(B) AKT-Luc/NICD injection; bioluminescence was measured every week. Livers
were extracted after 6 weeks of BLI. Statistical analyses were performed with
multiple Student's t-test. ***P < 0.001 (n = 5), and error bars are ± SEM.
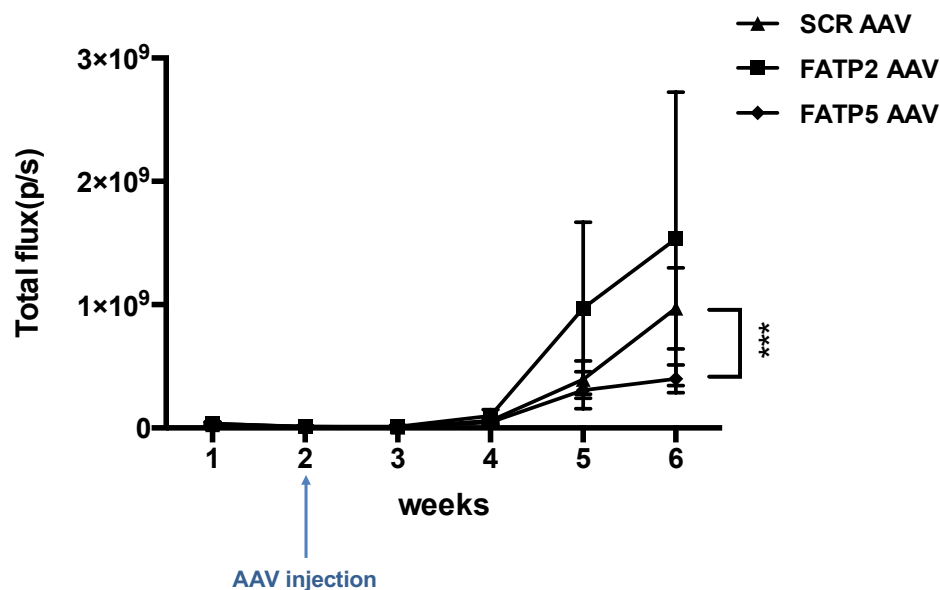
Figure. 3.7. FATP2 and FATP5 knockdown after the onset of tumor growth in ICC
Mice received AKT-Luc/NICD injection; AAV SCR, *FATP2*, and *FATP5* were injected 10 days later. Statistical analyses were performed with a two tailed Student's t-test. ***$P < 0.001$ (n = 4), and error bars are ± SEM.

Conclusion

The present work has extended our understanding of the role of FATP5 in hepatic carcinogenesis. To date, lipid metabolism studies in cancer have mostly focused on increased de novo lipogenesis as the source of fatty acids required for tumor cell growth and the role of FATPs in regulating tumor initiation and progression has not been studied so far. The present FFA uptake results demonstrated that the rate of FFA uptake is significantly decreased during the development of HCC, but not that of ICC. We also showed that the rate of FFA uptake decreased significantly during the development of HCC and the level of FATP2 and FATP5 expression was decreased drastically in HCC. This give us one possible explanation for the previous finding that ICC development is not dependent on FASN[131]. The expression of FATP2 and FATP5 in ICC occurs to the similar level as that observed in the wild type, suggesting that a sufficient level of fatty acid is available; as a result, the de novo synthesis of fatty acids is not required for tumor formation. We additionally showed that FATP5 knockdown suppresses ICC tumor formation, and that downregulation of FATP5 expression

delays tumor growth even after onset of ICC. Taken together, our findings indicate that FATP5 is a potential therapeutic target for the treatment of ICC.

Chapter 4

In vivo BLI reveals copper deficiency in a murine model of nonalcoholic fatty liver disease (NAFLD)

Significance and background

Copper is an essential transition metal in biology, playing a key role as a redox-active enzyme cofactor in various physiological processes, including antioxidant defense[132, 133], respiration[134, 135] and epigenetic modifications, with emerging regulatory roles in a variety of signaling networks[136-139]. Although copper has a variety of important biological roles, its redox activity requires tight regulation to prevent oxidative stress and free radical damage[140-143]. Genetic disorders that disrupt copper homeostasis can cause severe diseases, such as Menkes disease (copper deficiency) and Wilson's disease (copper overload)[144, 145]. Additionally, imbalances in physiological copper levels and organ distribution owing to genetic or dietary factors have been correlated with cancer, neurodegenerative diseases, and metabolic disorders, such as obesity, diabetes, and NAFLD[145-151].

Due to the importance of copper in biological systems, there is a need for bioanalytical tools that can sensitively and selectively monitor and track the copper level in biological samples. Taki et al have developed a copper-selective fluorescent probe for Cu^+ imaging in living cells, providing valuable information on the role of copper in various biochemical events[140, 152]. Hirayama et al. developed CS790, a copper probe with near-infrared emission, thereby making this probe useful for *in vivo* imaging[153]. This probe was successfully applied to a murine model of Wilson's disease wherein aberrant increases in visceral copper levels were detected *in vivo* and were correlated with elevated hepatic copper, as shown by *ex vivo* imaging of liver tissue. Although this work helped to highlight the presence of elevated Cu^+ in Wilson's disease, we aimed to create a new Cu^+ probe with a lower background signal that could be used for real-time, tissue-specific monitoring of both copper overload and depletion in whole animals. To this end, Chang's group developed a Cu^+-responsive probe for firefly luciferin BLI, in which light is generated through the luciferase-catalyzed conversion of the substrate D-luciferin to oxyluciferin. Luciferin-based BLI is an attractive molecular imaging modality due to its low background signal, highly efficient photon production, and good tissue penetration of the red-shifted emitted light[10, 12]. Furthermore, impressive bioengineering advances in luciferase-reporter systems have permitted the use of luciferin-based bioluminescent probes for tissue-specific imaging[3, 13, 154].

Here we present a novel bioluminescent reporter system for imaging copper in living animal model. Copper-Caged Luciferin-1 (CCL-1) is a tris(2-pyridyl)amine (TPA) ligand caged probe that generates D-luciferin upon oxidative

cleavage with Cu^+ for subsequent reaction with firefly luciferase to produce a bioluminescence. we demonstrated that CCL-1 could selectively detect exchangeable copper stores in living cells and under basal, copper-overload, or copper-deficient conditions in living mice. Furthermore, we applied the probe for tissue-specific detection of hepatic copper levels in transgenic mice expressing luciferase specifically in the liver. Finally, we utilized CCL-1 to monitor changes in hepatic copper levels in the progression of NAFLD using a diet-induced obesity model, demonstrating the potential of the probe to interrogate copper biology in metabolic disorders. These data establish CCL-1 as the first reported caged luciferin probe for monitoring metal fluxes in living animals and highlight the potential application of this research tool in the elucidation of pathogenic factors involved in metabolic disorders.

Results and discussion

This study was conducted in collaboration with Professor Chris Chang' lab at UC Berkekley. Dr Marie Heffern synthesized and provided all the compounds used in this study. All in vitro experiments were done by Dr Marie Heffern and in vivo experiments were conducted together.

Design and synthesis of CCL-1

Our strategy for *in vivo* detection of Cu^+ was based on a chemically modified firefly luciferin molecule that could be selectively uncaged by a Cu^+-mediated oxidative bond cleaving reaction (Fig.4.2). The Cu^+-selective uncaging reaction would lead to the release of luciferin, allowing for the detection of changes in labile Cu^+ levels through monitoring of the amount of luminescence The released luciferin produces bioluminescent light through enzymatic reaction of the firefly luciferase. In the absence of Cu^+, the modified luciferin is not albe to produce a luminescent signal. CCL-1 features a TPA ligand attached to firefly luciferin via an ether linkage. The tetradentate N_4-coordinating ligand has been previously implemented as a Cu^+-selective trigger incorporated into fluorescent probes[155]. Upon coordination of Cu^+ to the ligand, O_2-mediated oxidative C–O ether bond cleavage is expected to uncage and release the luciferin substrate, which will produce luminescence after an enzymatic reaction with luciferase. The synthesis of CCL-1 based on this design strategy is depicted in Fig 4.1.
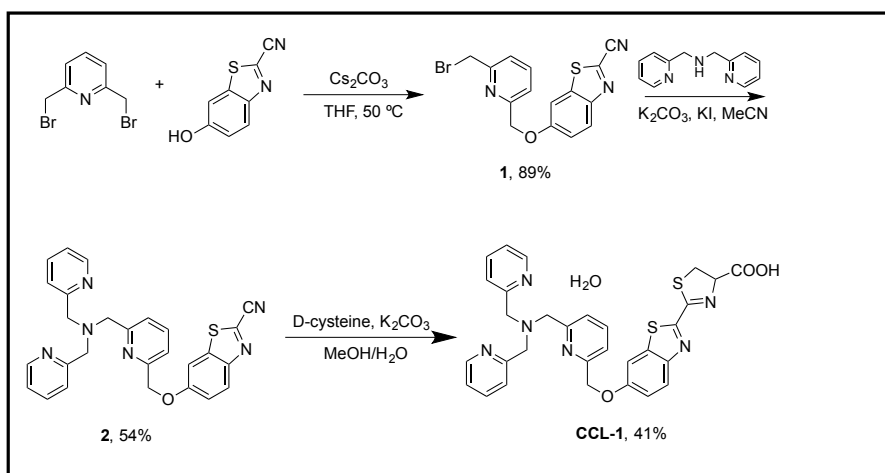
Figure 4.1. Synthesis of Copper-Caged Luciferin 1 (CCL-1)
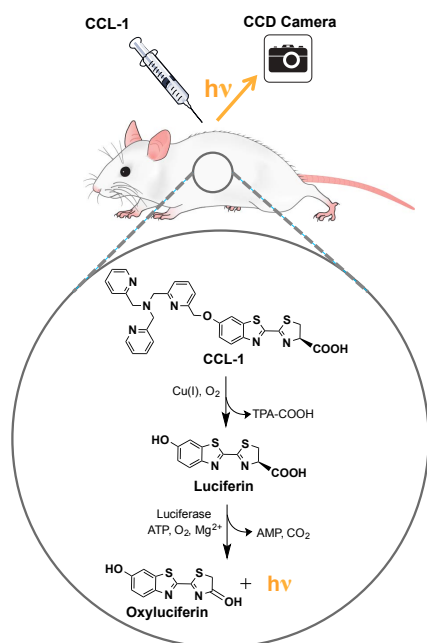
Figure 4.2. Design of Copper-Caged Luciferin 1 (CCL-1) through selective Cu$^+$-mediated oxidative release of the D-luciferin substrate

Reactivity and selectivity of CCL-1

Cu^+-mediated luminescence production from CCL-1 was initially measured in aqueous buffer (50 mM Tris at pH 7.4, 5 mM glutathione). First, a 5 μM solution of CCL-1 was incubated with various concentrations of Cu^+ (0.5–50 μM) for 1 h, followed by addition of recombinant firefly luciferase. Luminescent signal emission was measured with a plate reader and compared to the control condition without Cu^+. As shown in Fig 4.3.A, a good correlation between the Cu^+ concentration and the total bioluminescent signal was observed up to 5μM Cu^+ (one equivalent) indicating that CCL-1 could reliably detect different levels of Cu^+.

Metal selectivity of CCL-1 towards Cu^+ was also examined. As shown in Fig 4.3B, CCL-1 exhibited high Cu^+ selectivity over other biologically abundant metals, such as Mg^{2+}, Ca^{2+}, and Zn^{2+}, as well as other common 3d transition metal ions. A slight increase in luminescent intensity was observed in Co^{2+}; however, while biological concentrations of loosely bound ionic Co^{2+} are not well-studied, the concentration tested here is not considered physiologically relevant as most Co^{2+} are found tightly bound to proteins.[156] In order to make the intracellular reducing environment, 5mM GSH was added to the buffer used in the tests. Under such conditions, Cu^{2+} was readily reduced to Cu^+, and a comparable luminescent enhancement (approximately 70-fold) was observed.
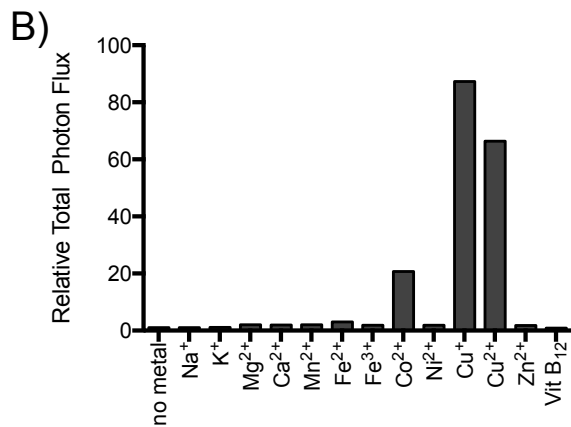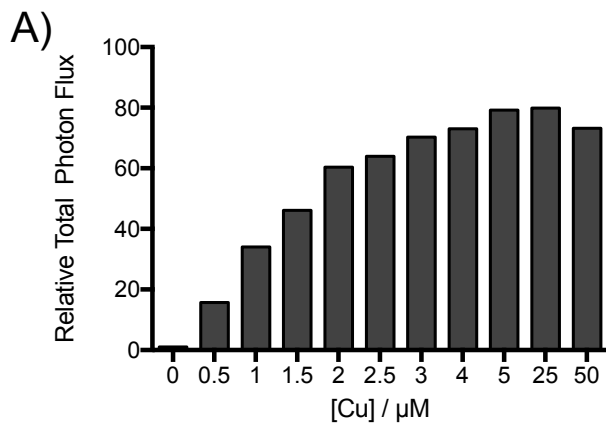
Figure 4.3. CCL-1 selectively responds to Cu$^+$ and can measure dynamic changes in Cu$^+$ levels in living cells.
Relative bioluminescence response of CCL-1 (5 µM, in 50 mM Tris, pH 7.4, 5 mM GSH) after 1 h incubation with A) varying concentrations of Cu+ and B) various biologically relevant s-block (1mM) and d-block (100 µM) of various biologically relevant metal ions and cobalamin (Vitamin B12). Signals are integrated over 1 h and expressed relative photon fluxes normalized to CCL-1 bioluminescence with no metal ion treatment.

CCL-1 detected changes in labile copper in living cells

After confirming that CCL-1 could reliably detect different Cu^+ levels in aqueous buffer, we tested whether this probe could also detect changes in labile Cu^+ levels in live cells. Two luciferase-expressing stable cell lines, PC3M-luc and LNCaP-luc, were used in the experiments. The cells were incubated with different concentrations of $CuCl_2$ for 24 h to elevate the intracellular copper level. After 24 h, the cells were washed and treated with CCL-1. The bioluminescent signal increased with increasing concentrations of $CuCl_2$ in the incubation medium, indicating the dependence of the signal on copper (Fig 4.4A, 4.4B). In addition, the signal was decreased to the basal level when the cells were treated with the intracellular Cu^+ chelator tris(2-ethylthio)ethylamine (NS3'), before addition of CCL-1, indicating that the increase in bioluminescence was dependent on copper and that CCL-1 could detect different levels of labile Cu^+ in living cells. Moreover, cells treated only with NS3' showed a significant decrease in bioluminescence (Fig 4.4C) demonstrating that CCL-1 is sensitive to detect alterations in the endogenous level of copper.
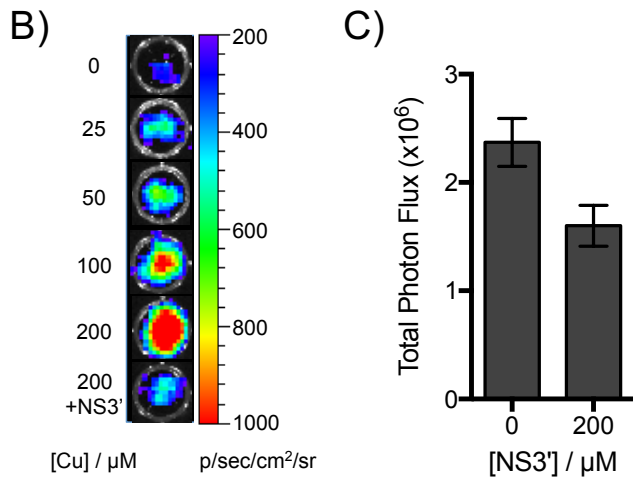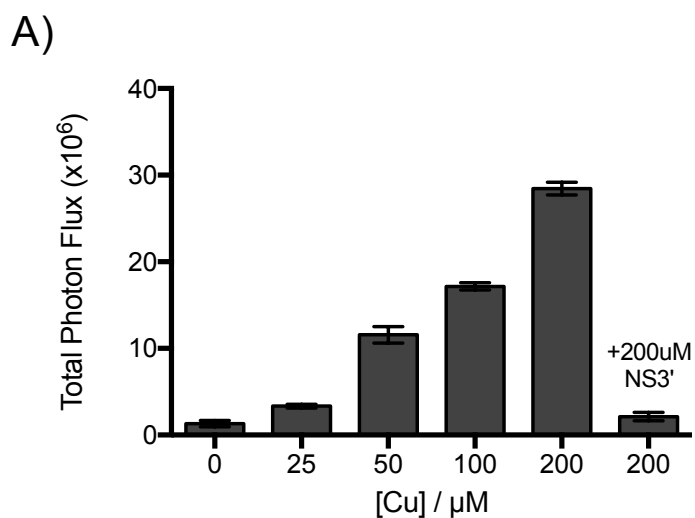
Figure 4.4. CCL-1 selectively responds to Cu$^+$ and can measure dynamic changes in Cu$^+$ levels in living cells

A) Bioluminescent signals from PC3M-luc cells probed with CCL-1. Cells were supplemented with CuCl$_2$ for 24 h, followed by addition of CCL-1 (25 µM) ± the membrane-permeable copper chelator NS3' (200 µM). Total photon flux was integrated over 2 h. Error bars are ± SD (n = 3).

B) Representative images of PC3M-luc cells treated with CuCl$_2$ and imaged with CCL-1. C) Bioluminescent signals from PC3M-luc cells loaded with CCL-1 (50 µM) ± NS3' (200 µM). Total photon flux was integrated over 2 h. Error bars are ± SD (n = 3).

CCL-1 detected changes in exchangeable copper in living mice

Given the ability of CCL-1 to detect both exogenous and endogenous copper in cells, we next measured copper in firefly luciferase-expressing transgenic mice (FVB-luc+). Animals were first treated with vehicle or $CuCl_2$ (3 mg/kg) 2 h prior to injection of CCL-1. Following the CCL-1 injection, light production was monitored for 1 h through imaging with a sensitive CCD camera, and the total photon flux from each animal was measured (Fig 4.5). Animals pretreated with copper showed a robust, 9-fold increase in bioluminescent signal from CCL-1. To determine whether this change in signal was dependent on copper, another group of animals treated with $CuCl_2$ was also treated with a copper chelator, ATN-224 (5 mg/kg), prior to injection of CCL-1. These animals exhibited a bioluminescent signal comparable to that of the control group, indicating that CCL-1 can be used to monitor fluctuations in copper levels in vivo.

Since the liver is the central organ for copper metabolism, we next decided to image hepatic copper with CCL-1 in transgenic mice express luciferase exclusively in their liver (L-Luc mice). As in the FVB-luc+ mice, the L-Luc mice were first treated with vehicle, $CuCl_2$ (3 mg/kg), or ATN-224 (5 mg/kg) in addition to $CuCl_2$ (Fig 4.6). Copper pretreatment resulted in a 7-fold increase in bioluminescent signal from CCL-1, and this increase was attenuated by treatment with ATN-224, demonstrating the ability of CCL-1 to detect increases in hepatic copper levels. Because several metabolic disorders have been reported to result in copper deficiency, we treated another group of mice with ATN-224 alone (30 mg/kg) prior to imaging so as to reduce basal copper levels (Fig 4.6). A 6.5-fold decrease in bioluminescent signal from the vehicle treatment was observed following chelator treatment, indicating that CCL-1 could detect both depletion and overload of hepatic copper.
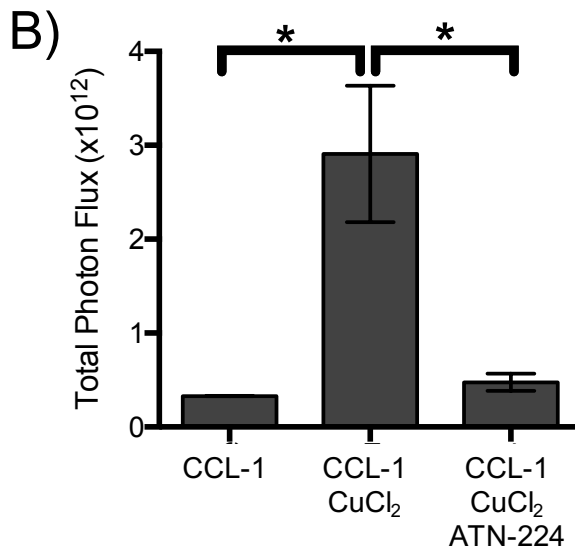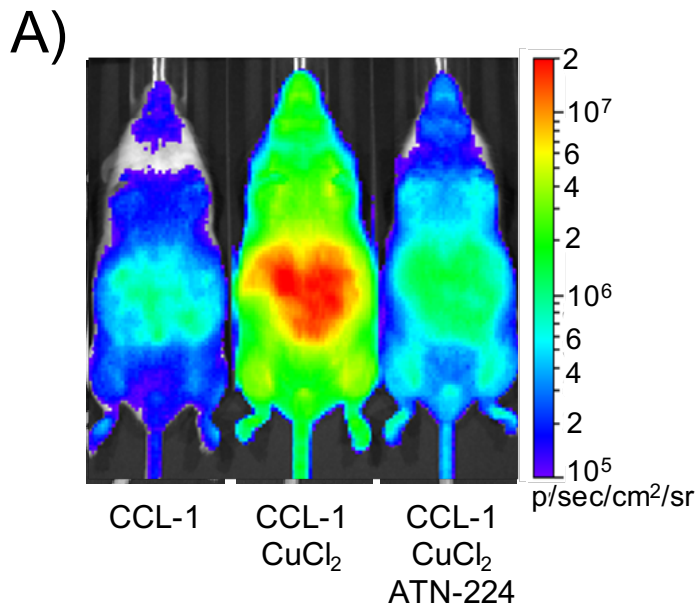
Figure 4.5. CCL-1 monitors labile copper dynamics in luciferin-expressing mice

FVB-luc[+] mice were injected (i.p.) with CCL-1 (0.2 μmol) after i.p. injection of vehicle, $CuCl_2$ (3 mg/kg), or both $CuCl_2$ (3 mg/kg) and ATN-224 (5 mg/kg). Injection of $CuCl_2$ and ATN-224 were performed 2 h and 10 min prior to injection CCL-1, respectively. A) Representative images of FVB-luc[+] mice injected with CCL-1. B) Total photon flux, 0–60 min post-injection. Statistical analyses were performed with a two-tailed Student's *t*-test. *P < 0.05 (n = 3-5), and error bars are ± SEM.
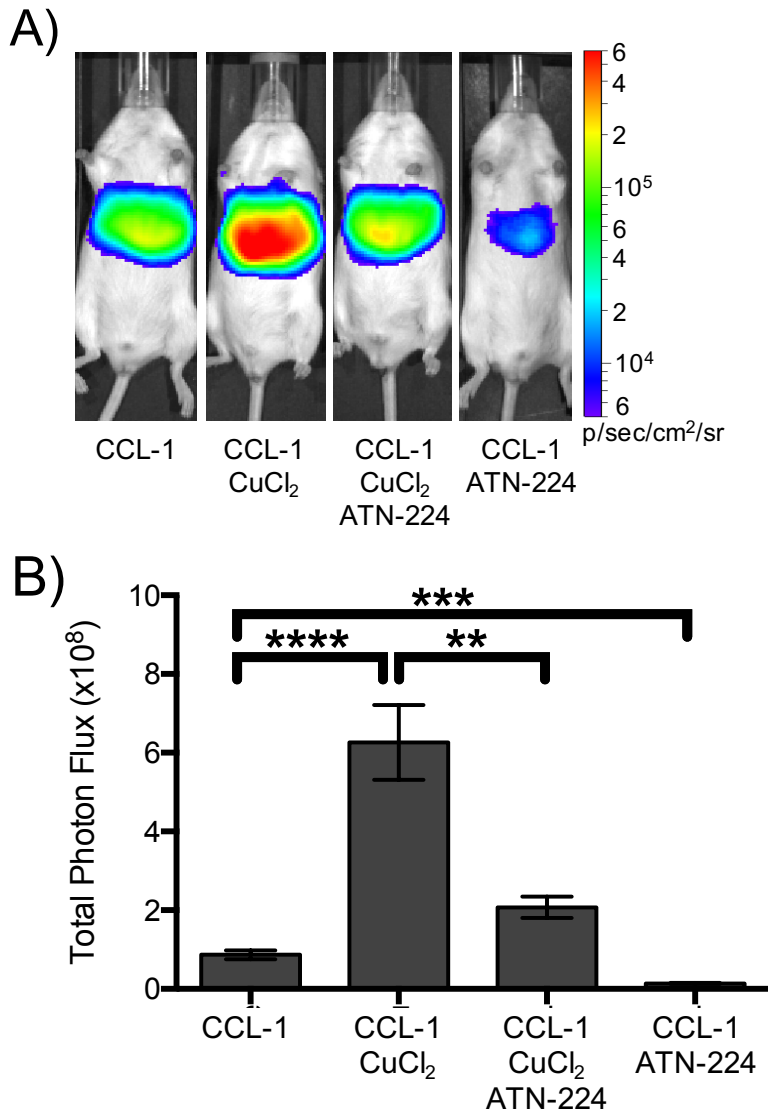
Figure 4.6. CCL-1 monitors Cu$^+$ dynamics and can detect endogenous, basal labile Cu$^+$ levels in L-Luc mice

L-Luc mice were injected (i.p.) with CCL-1 (0.1 µmol) after i.p. injection of vehicle, CuCl$_2$ (3 mg/kg) alone, both CuCl$_2$ (3 mg/kg) and ATN-224 (5 mg/kg), or ATN-224 (30 mg/kg) alone. Injections of CuCl$_2$ or ATN-224 alone were performed 2 h prior to injection of CCL-1. Mice injected with both CuCl$_2$ and ATN-224 were injected 2 h and 10 min prior to injection of CCL-1, respectively. A) Representative images of L-Luc mice injected with CCL-1 under various conditions. B) Total photon flux, 0–60 min post-injection. Statistical analyses were performed with a two-tailed Student's t-test. **$P \leq 0.01$, ***$P \leq 0.001$ ****$P \leq 0.0001$ (n = 3-7), and error bars are ± SEM.

CCL-1 revealed copper deficiency with alterations in copper transport proteins in a diet-induced murine model of NAFLD

After establishing that CCL-1 could be used to monitor fluctuations in hepatic copper pools *in vivo*, we sought to apply the probe to interrogate changes in hepatic copper levels in a metabolic disease model. Copper availability and regulation has been linked to lipid and glucose metabolism, and clinical evidence has linked inadequate copper supply to the severity of NAFLD[146, 157, 158]. To this end, 6–8-week-old liver-luc mice were fed a high-fat diet (HFD) to induce NAFLD or normal chow for 8 weeks with weekly monitoring of food intake and weight gain. Mice were imaged weekly with D-luciferin to monitor liver size, followed by injection of CCL-1 2 days later to measure hepatic copper. Interestingly, a notable decrease in signal from CCL-1 (normalized to the D-luciferin signal) was observed in the liver-luc mice fed the HFD for 8 weeks (Fig 4.7.A); this decrease was not observed in mice fed normal diets.

At the end of the 8-week feeding period, compared with animals fed normal chow, animals fed the HFD exhibited significantly increased body weights (~45%; Fig 4.8.B). Whole-body glucose clearance after intraperitoneal (i.p.) injection of glucose (2 mg/g) was monitored to evaluate glucose tolerance (Fig 4.8.A). Although the mice fed normal chow showed a reduction in glucose back to the basal level after 2 h, the HFD mice displayed significant impairment in glucose metabolism, with elevated glucose levels throughout the test (85 mg/dL above basal levels), validating disease induction.

Ex vivo analysis of tissues from the two groups of mice was performed to determine how the disease model affected copper levels. We quantitatively assessed total copper levels in the livers of the HFD mice and mice on normal chow using inductively coupled plasma mass spectrometry (ICP-MS) analysis. Copper content was also measured by ICP-MS analysis in the brains, intestines, and kidneys for comparison. In agreement with previous studies, the analysis revealed a relative deficiency in hepatic copper levels in the HFD mice as compared with that in mice fed normal chow, verifying the copper decrease observed in the imaging of HFD mice with CCL-1 (Fig 4.9.). Interestingly, the HFD mice exhibited higher copper levels in the kidney than mice fed normal chow. Previous studies revealed copper dysregulation in diabetic patients and animal models has been reported to manifest as copper overload in the kidneys but copper deficiency in other tissues, suggesting potential similarities in the mechanism and effects of copper imbalance observed in this NAFLD model[149, 158]. Taken together, these data demonstrated the imbalance in copper levels in our mouse model of NAFLD, resulting in a deficiency in hepatic copper; importantly, this imbalance could be monitored in living mice through BLI with CCL-1. However, copper levels in high fat and low fat diets were significantly different and follow up studies with Cu^+ matched content diets will need to be performed to confirm our results
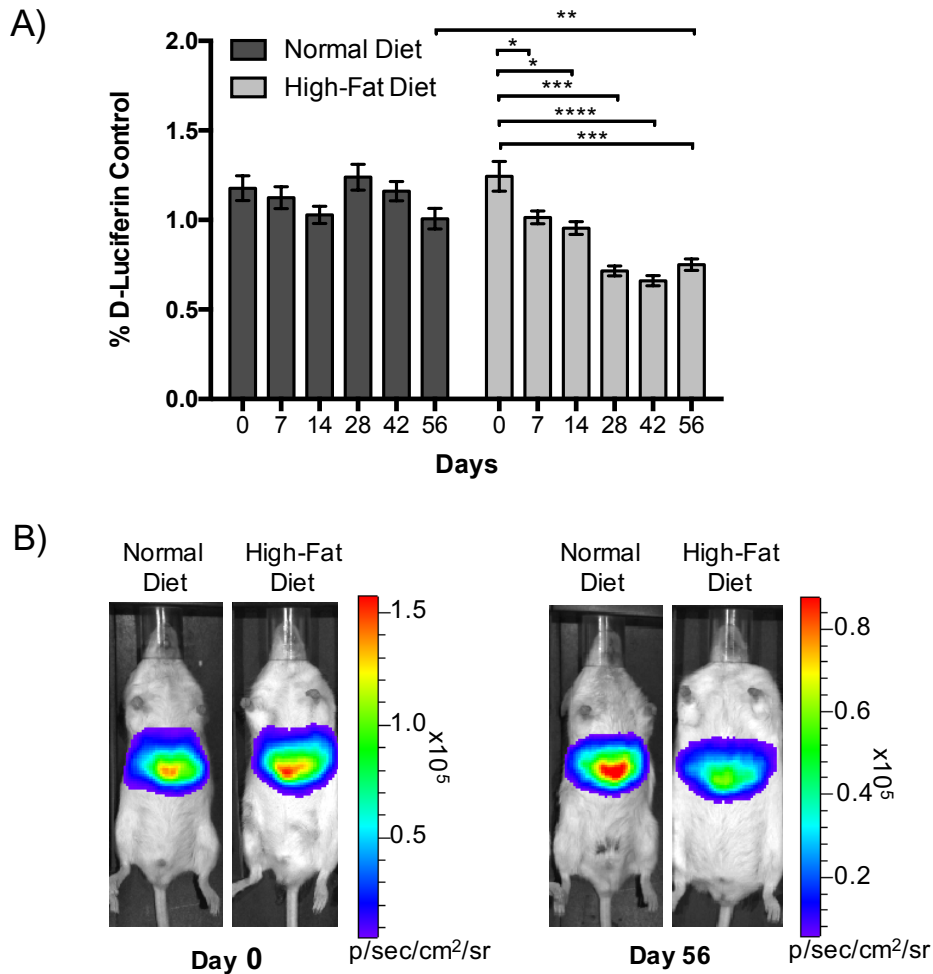
Figure 4.7. CCL-1 imaging reveals hepatic copper deficiency in a diet-induced murine model of NAFLD

A) Bioluminescent signal from CCL-1 (normalized to D-luciferin) of L-Luc mice placed on a high-fat diet or normal feeding conditions. Mice were imaged biweekly after i.p. injection of D-luciferin followed by CCL-1 2 days later. Error bars are ± SEM (n ≥ 9) and statistical analyses were performed with a two-tailed Student's *t*-test where **P ≤ 0.01, ***P ≤ 0.001 ****P ≤ 0.0001. B) Representative images of mice from high-fat diet and normal diet groups prior to the study (day 0) and at the end of the 8-week feeding period (day 56)

A)

B)
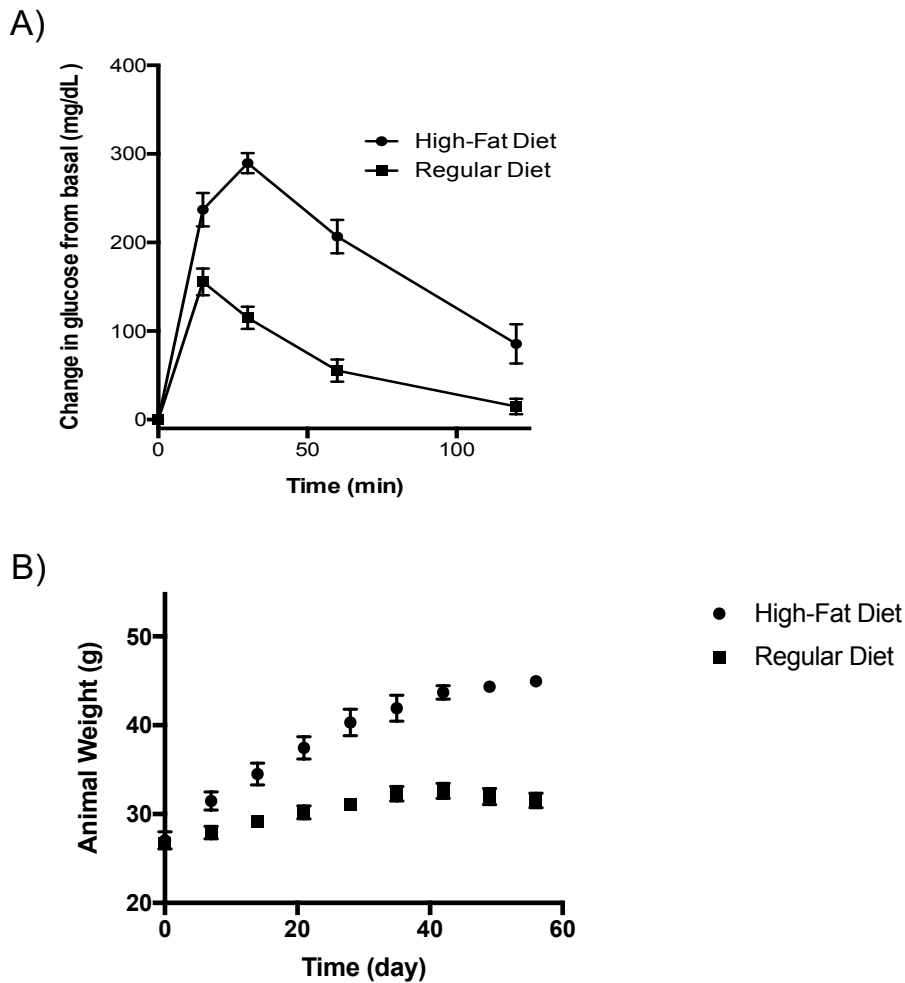
Figure 4.8. Development of diet induced NAFLD in L-Luc mice
A) Glucose clearance test to monitor glucose intolerance of the two groups of mice following i.p. injection of 200 mg/dL of glucose. Glucose was injected after blood glucose levels were measured at time = 0 min. Data are expressed as changes in glucose levels from basal levels (levels measured at time = 0 min, prior to glucose injection). Error bars are ± SEM (n = 6). B) Animal weights were monitored weekly for the two groups. Diets contained 17.6 ± 0.2 µg Cu/g in the normal diet and 8.4 ± 0.2 µg Cu/g in the high-fat diet. Error bars are ±SEM (n = 6).
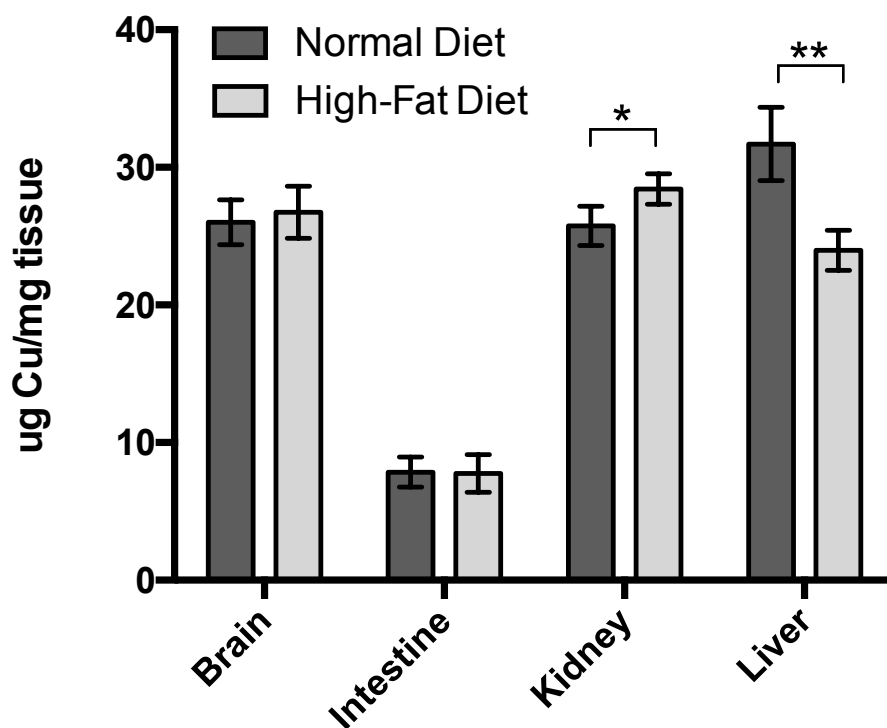
Figure 4.9. ICP-MS analysis of total copper in brain, intestine, kidney, and liver tissues from high-fat diet and normal diet groups
Error bars are ± SEM (n = 6 or 7) and statistical analyses were performed with a two-tailed Student's *t*-test where *P ≤ 0.05, **P ≤ 0.01.

Conclusion

In this study, we evaluated CCL-1, a new generation bioluminescent copper-responsive probes as an ideal tool for copper dynamic studies. CCL-1 is selective to Cu+ over a wide range of biologically relevant and abundant metal ions, and its high sensitivity enables tracking real-time changes in labile, loosely bound copper pools in cells and live animals. Using this unique chemical technology to tissue-specific *in vivo* copper imaging in animal models, we identified an imbalance in copper homeostasis in a diet-induced murine model of NAFLD. Because this method enables monitoring of fluctuations in copper levels in the same animals over time, we are able to directly observe a decrease of hepatic copper level in vivo at early stages of high-fat feeding before many symptoms of NAFLD display suggesting that changes in copper metabolism may lead to onset of the disease and progression

In conclusion, CCL-1 is a novel tool for studying copper biology in various biological systems. This novel copper imaging probe, which can function at both the cellular and organism levels, will provide unique opportunities to study

47

biological properties of copper and expand our understanding of the role of copper in life.

Chapter 5

A Biocompatible in Vivo Ligation Reaction and Its Application for Noninvasive Bioluminescent Imaging of Protease Activity in Living mice

<u>Significance and background</u>

To study biomolecules in their native environments, biocompatible reactions have been developed in the past decade[159]. Components of biocompatible reactions should react rapidly and selectively in the presence of all other functionalities present in a living system. However, only a small portion of these reactions, such as copper-free cyclooctyne-type cycloaddition[160-162], Staudinger ligation[163-165], and recently reported tetrazine-alkyne reactions[166-169] can be used in live cells because they do not require the use of toxic metal catalysts.

Also, complexity of a system increases beyond that of living cells to living animals, there are many more requirements for successful biocompatible reactions. Previous studies have shown that only the Staudinger ligation worked in live mice because it's reagents contain low toxicity, favorable pharmacokinetics, and an absence of nonspecific binding with other biomolecules[159, 161]. But the phosphine reagents used in Staudinger ligation have certain liabilities such as susceptibility to oxidation by molecular oxygen[170]. Also Staudinger ligation has a relatively slow reaction rate, compromising its ability to monitor rapid biological processes in vivo[171].

We are primarily interested in the reaction of D-cysteine with 6-hydroxy-2-cyanobenzothiazole (OH-CBT) as the final step of d-luciferin synthesis[172]. Since, N-terminal cysteine residues have frequently been used in protein engineering, previous studies reported the assembly of polymers in physiological solutions and selectively label proteins on N-terminal cysteines for site-specific labeling and modification [173-176]. Remarkably, the rate of this reaction has been reported to be three orders of magnitude faster than the Staudinger ligation[175]. However, this reaction has not been used in live mice.

The reaction between d-cysteine and CBTs has great potential for use in conjunction with BLI, the most sensitive in vivo currently available for living animals, because the reaction can yield D-luciferin, a substrate for firefly luciferase. 6′-hydroxy (6′-amino) group of D-luciferin is crucial for bioluminescence emission and therefore modification (caging) methods at the hydroxyl group has been developed to control the light emission procedure. The caged luciferin is not able to react with luciferase until the cage cleaved by corresponding enzymes or biomolecules[154]. BLI using caged luciferin probes has been used to directly measure enzymatic activities such as β-galactosidase[35], caspases[36, 37], furin[39], and β-lactamases[40] in living animals. Because cysteine

49

derivatives are easier to synthesize and have high stabilities to light and pH, these precursors can be exploited as another probes for in vivo imaging[177-180].

In this study, we demonstrated that D-cysteine and CBTs can selectively react with each other to generate a luciferin substrate for firefly luciferase in living cells or animals. Moreover, since both CBT and D-cysteine can be modified with different caging groups, Dubikovskaya's group developed a caged D-cysteine as a substrate for caspase 3 for the real-time imaging of caspase activity. We showed that this "split luciferin" ligation reaction using caged D-cysteine enables simultaneous detection of caspase 3 activity both in vitro and in vivo. Thus, this study showed the potential of the D-cysteine and CBTs reaction as a novel biocompatible reaction to study more complex biological processes simultaneously in living cells or animals.

Results and discussion
This study was conducted in collaboration with Professor Elena A. Dubikovskaya's group at Swiss Federal Institute of Technology of Lausanne. Aurelien Godinat (Graduate student) synthesized and provided all the compounds used in this study. All in vitro experiments were done by Aurelien Godinat.

In vitro formation of D-aminoluciferin in physiological solutions.
We first tested whether OH-CBT and NH_2-CBT could form their respective luciferins directly in a biocompatible environment (Fig 5.1). Thus, we incubated the NH_2-CBT compound with either D- or L-cysteine in a buffer containing luciferase enzyme and measured light emission. Importantly, the signal produced from the sample that had both NH_2-CBT and D-cysteine was 10-fold higher than the signals obtained from samples containing either NH_2-CBT alone or NH_2-CBT plus L-cysteine (Fig 5.2). These results indicated the reaction of NH_2-CBT and D-cysteine can from D-luciferin analogs in physiological buffers that could directly produce photons of light in the presence of luciferase.
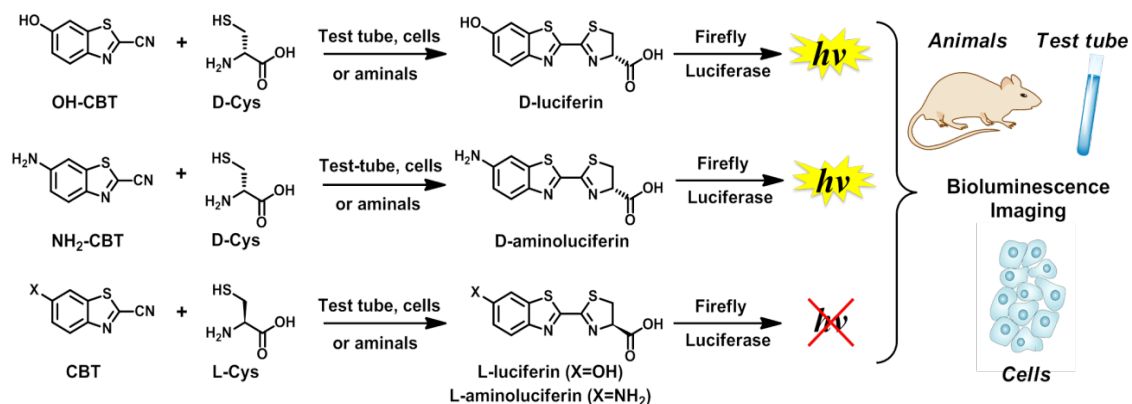
Figure 5.1. Overall schematic of luciferin ligation reaction between D- or L-cysteine and hydroxy- or amino- cyanobenzothiazole derivatives (OH-CBT and NH₂CBT) in various biological environments
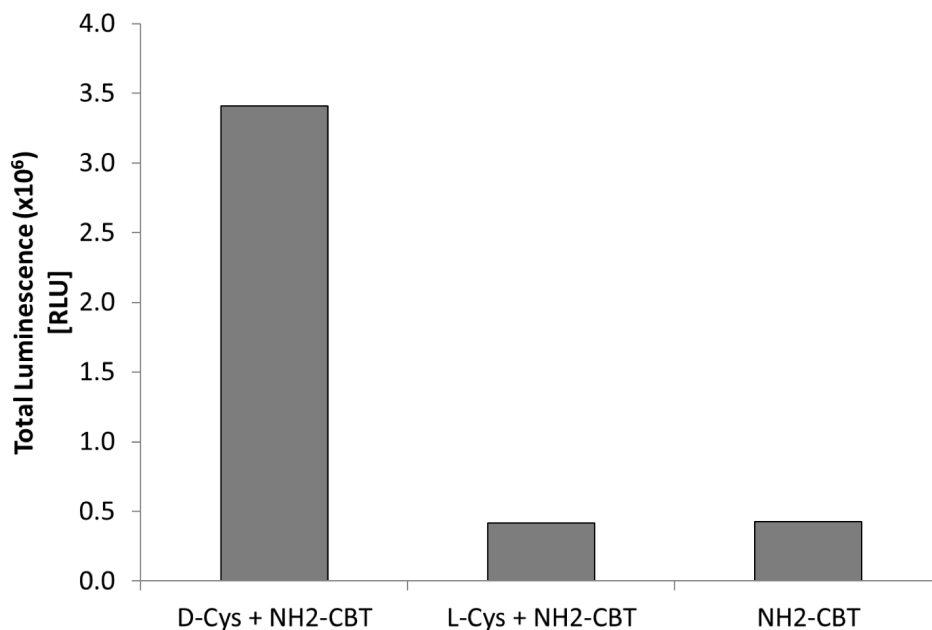
Figure 5.2. *In vitro* formation of D-luciferin
Total bioluminescent signal intergrated over 2 h observed from incubation of 23 µL of a NH₂-CBT solution (50 mM in MeOH) and either 50 µL of a D-cysteine solution (16 mM in PBS), L-cysteine solution (16 mM in PBS), or PBS along.

Imaging and quantification of split luciferin ligation reaction in living cells.

Next, we tested whether OH-CBT could form their respective luciferins directly in live cells. We used a firefly luciferase expressing stable cell line termed (SKOV3-luc-D3) based on SKOV3 cells. Cells were treated with OH-CBT and signal was monitored using a cooled CCD camera. OH-CBT treatment produced only a baseline level of signal (Fig 5.3). Also, cells treated with both OH-CBT and L-cysteine produced the same background signal as cells treated with OH-CBT alone (Fig 5.3). In contrast, cells treated with D-luciferin yielded a robust signal that was significantly higher than background (Fig 5.3).

We next incubated the same cells with OH-CBT and D-cysteine. Interestingly, the amount of light produced by cells treated with both D-cysteine and OH-CBT reagents significantly exceeded the signal from an equivalent amount of D-luciferin (Fig. 5.3). Figure 5.3B demonstrates the overall total photon flux over 1 h, obtained after integration of the area under the corresponding curves (Fig 5.3A).

Interestingly, significant more light was detected in cells with OH-CBT and D-cysteine than in D-luciferin treated cells. Because this may be due to the differences in permeability or stability of each compound, we conducted an experiment to test this hypothesis. We first pre-incubated cells with D-cysteine followed by washing and addition of a CBT and then strong signal was observed. The produced signal was 30% of the signal produced by the incubation with simultaneous treatment of both reagents. In addition, these signals are 20% higher than the signal from equimolar concentration of D-luciferin (Fig 5.3B). 20minutes incubation of D-cysteine produced stronger signal than D-luciferin alone suggested that D-cysteine may have much higher permeability than D-luciferin or higher stability of under the physiological environment[177-182].
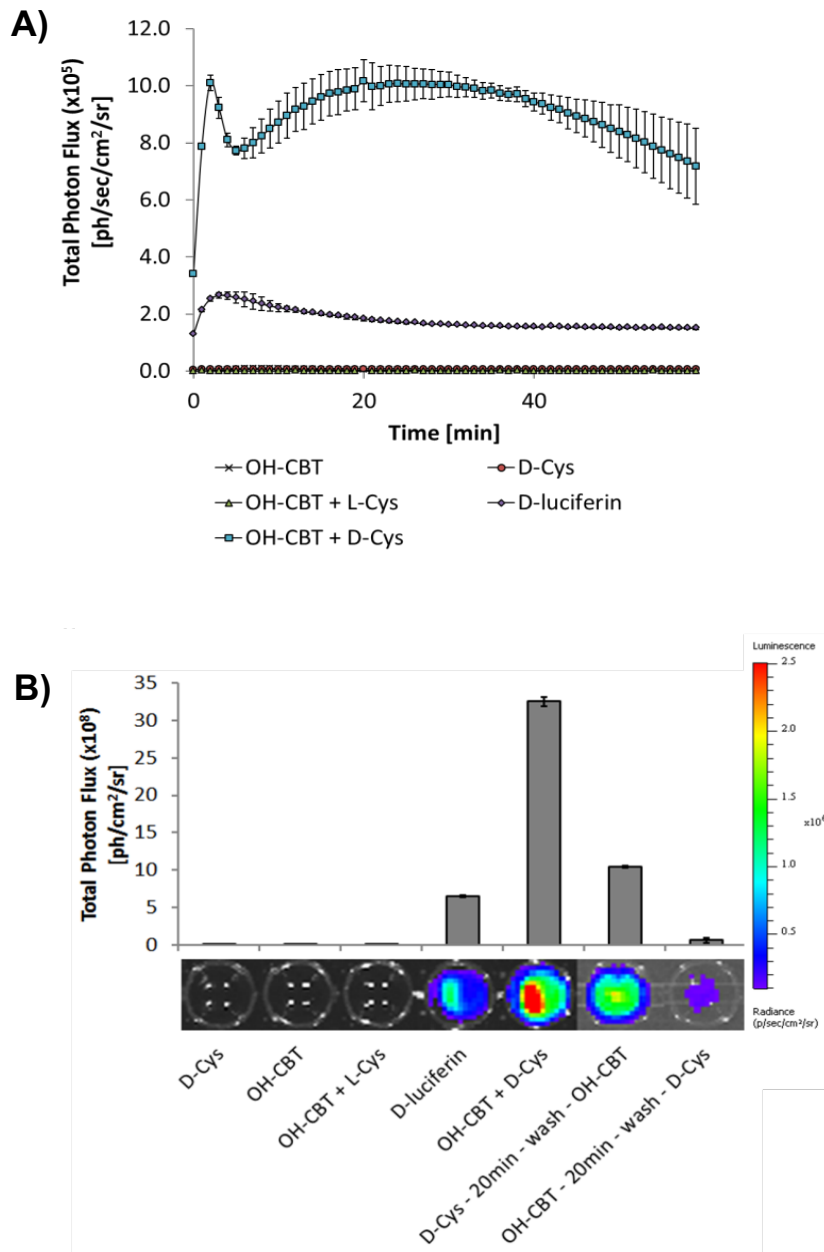
Figure 5.3. Luciferin ligation reaction in live cells
A) Observed bioluminescence produced as a function of time from SKOV3-Luc-D3 live cells, incubated with corresponding reagents. Error bars are ± SD for three independent measurements. B) Total photon flux produced in 1 h from live SKOV3-Luc-D3 cells incubated with corresponding reagents, calculated by integrating the area under corresponding kinetic curves in Fig 5.3A. Error bars are ± SD for three independent measurements.

Real time imaging and quantification of split luciferin ligation reaction in living animals.

Next, we determined whether both luciferin precursors could react directly in living animals to form their respective luciferins (Fig 5.4, 5.5, 5.6). We used transgenic animals that expressed luciferase in a whole body (FVB-luc+ mice) to visualize and measure the luciferin production.

We first injected the mice with either OH- or NH_2-CBT alone and measured the total photon flux to use as background signal (Fig 5.5, 5.6). When we repeated this experiment with the addition of an equimolar amount of D-cysteine 10 min post-injection of CBTs, a robust signal was obtained only a few minutes after injection, suggesting the relatively fast rate of conversion of the reagents compared with the full D-luciferin scaffold (Fig 5.6A). Notably, the signal produced from animals injected with D-cysteine and NH_2-CBT was 2.4 times higher than the signal from the corresponding OH-CBT precursor (Fig 5.6.B), consistent with previously reported data describing the relative light output between D-aminoluciferin and D-luciferin[24, 179, 181, 183].

In contrast to the cell study, the total light outputs produced by animals injected with D-cysteine and equimolar amounts of OH-CBT and NH_2-CBT were 10% and 17% of the overall signal obtained from the D-luciferin-injected control group, respectively (Fig 5.6B). This change in ratio of signal production between animals and cells could be due to the fact that whole organisms have a much more complex environment than cells, which are gown in a static environment in culture dishes.

To find the optimal ratio for the split luciferin ligation reaction in living mice, we tested different ratio of precursors of luciferin. We tested injection of one equivalent of OH-CBT or NH_2-CBT and 10 equivalents of D-cysteine. The resulting signal was 7- and 6-fold increased for OH_CBT and NH_2-CBT respectively, compared with the light output from injection 1:1 ratio (Fig 5.6). The total photon flux from the animals injected with a 1:10 ratio of OH-CBT and D-cysteine was half of the signal obtained from the D-luciferin control group while a 1:10 ratio of NH_2-CBT and D-cysteine produced an equivalent amount of light as the D-luciferin group (Fig 5.6).
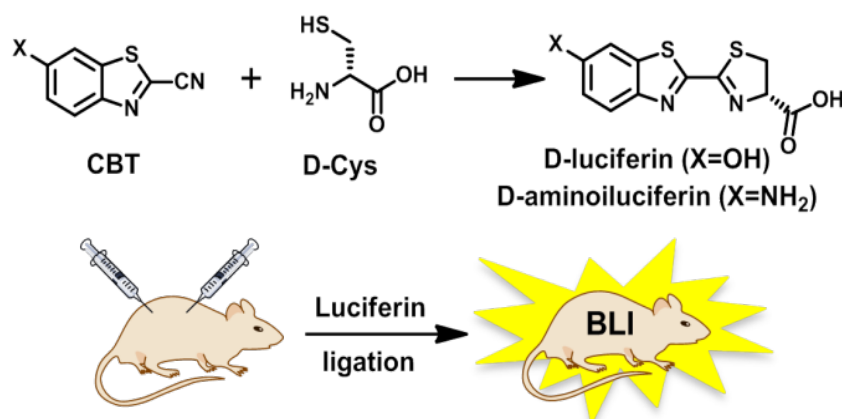
Figure 5.4. Overall schematic of *In situ* formation of D-luciferin or D-aminoluciferin in living transgenic reporter animals
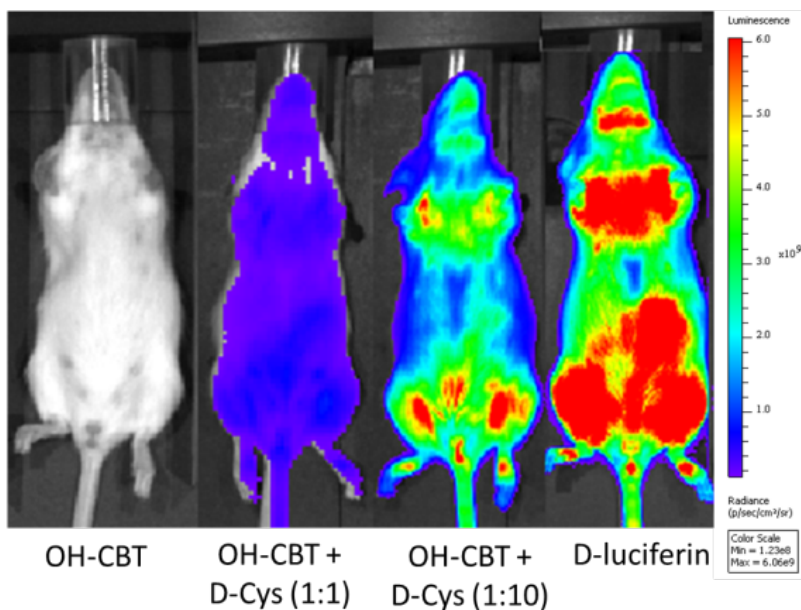
Figure 5.5. Luciferin ligation reaction in living mice.
Observed bioluminescence from luciferase transgenic mice as a function of time after IP injection of hydroxy-CBT; D-Cysteine and hydroxy-CBT in equimolar concentrations (1:1); D-Cysteine and hydroxy-CBT in 1:10 ration; and D-luciferin (all equivalent to 75mg/kg concentration of D-luciferin in 100 µL of PBS).
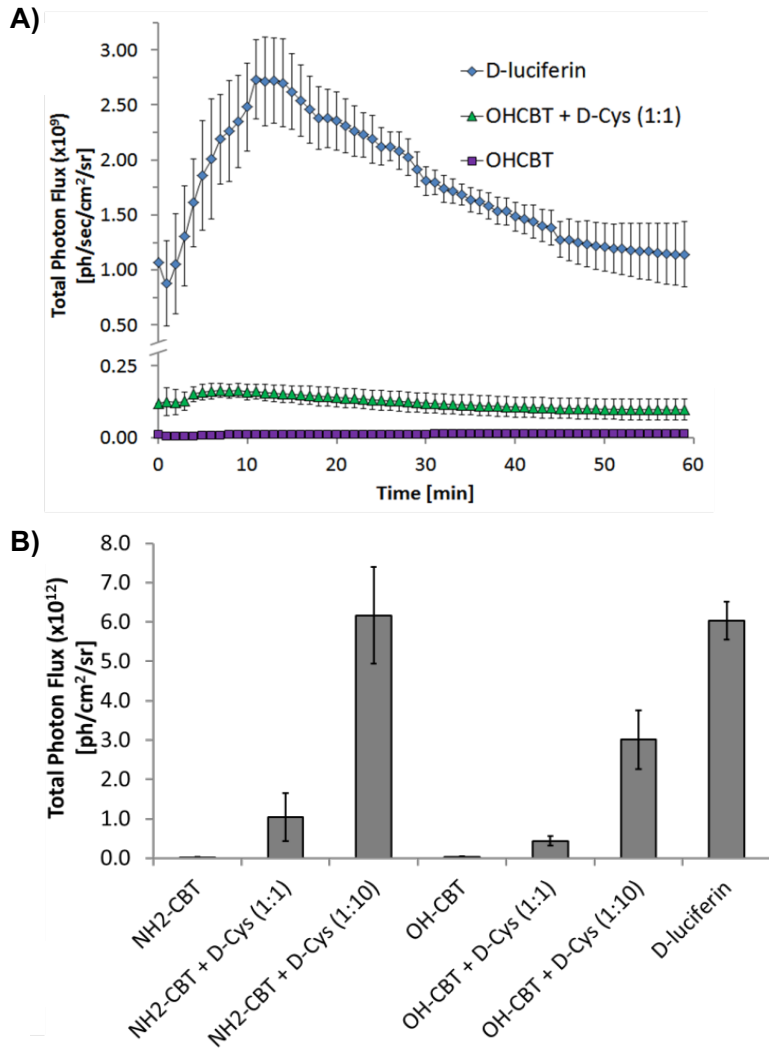
Figure 5.6. Luciferin ligation reaction in living mice
A) Representative image of mice 15 min post-injection of hydroxy-CBT, hydroxy-CBT + D-Cysteine (equimolar concentration), OH-CBT + D-Cysteine (1:10 respective concentration ratio) and D-luciferin. B) Total photon flux integrated over 60 min from resulting bioluminescent signal after IP injection of corresponding reagents (D-Cysteine and NH_2-CBT, D-Cysteine and OH-CBT in 1:1 and 1:10 ratios as well as D-luciferin). Error bars are ± SD for five measurements.

In vitro imaging of activity of caspase 3 proteases.

Because the structure of D-cysteine makes it suitable for being caged as a substrate for proteases including caspase 3, we examined whether luciferin ligation reaction between the caged D-cysteine and CBT can be used as a tool to detect specific protease activity. To test the viability of this approach, we chose to work with caspase 3 which plays important roles in several human pathologies including apoptosis[184-186].

DEVD-containing peptides (Asp-Glu-Val-Asp) are known to be selective substrates for caspase 3[187]. Because caspases 3 is known to cleave at the N-terminal end of their corresponding protease-specific amino acid sequences, we synthesized D-cysteine with these peptides at the N-terminal end, yielding L-(Asp-Glu-Val-Asp)-D-Cys (DEVD-[D-Cys]). DEVD-[D-Cys] were then incubated with increasing concentrations of their corresponding proteases, followed by addition of CBT and luciferase buffers. If the protease is active and can recognize its specific peptide sequence, free D-cysteine would be produced in the course of the reaction. Therefore, addition of CBT and luciferase enzyme would consequently produce significant light signal with more light output from samples having higher protease concentrations (Fig 5.8). The highest signal produced from DEVD-(D-Cys) peptide after the incubation with caspase 3 reached 50% of the light signal from the free D-cysteine control (Fig 5.8). This result confirmed that the DEVD-(D-Cys) peptide was a good substrate for caspase 3.
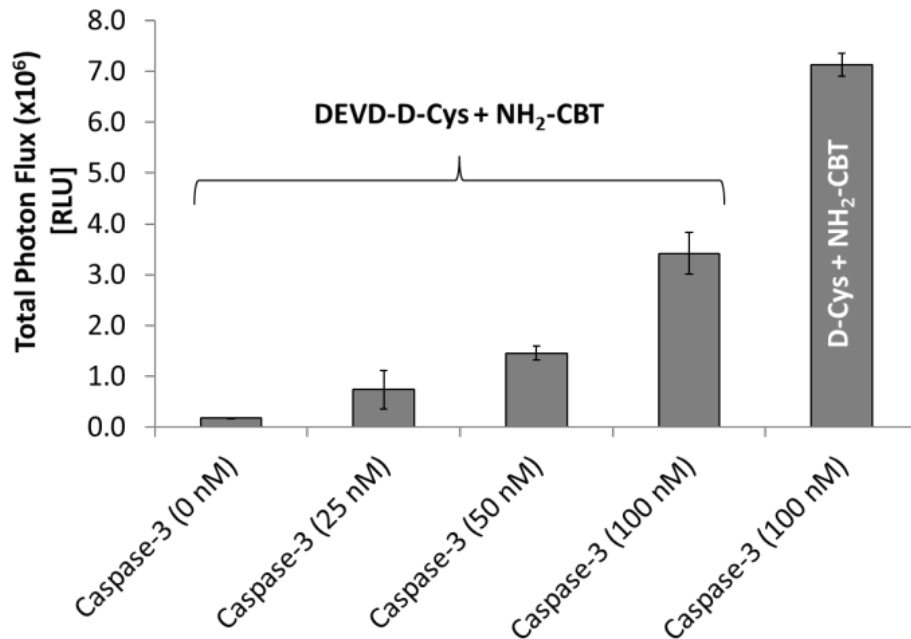
Figure 5.7. I*n Vitro* Imaging of Activity of Caspase 3 Proteases
Test tube assay of caspase-3 activity imaging with DEVD-D-Cys peptide and amino-CBT. Total bioluminescent signal integrated over 2h from DEVD-D-Cys peptide or D-cysteine control (200 µM) after incubation with increasing Caspase-3 concentrations (25, 50 and 100 nM) over 3h at 37°C. before addition of amino-CBT (400 µM) followed by 1 hr incubation at 37°C and subsequent imaging after addition of luciferase buffer. Error bars are ± SD of two measurements.

Real time non-invasive imaging of caspase 3 activities in living animals.

We next tested whether DEVD-(D-Cys) can detect caspase3 activity in live FVB-luc+ mice. We induced caspase 3 activity by injecting the animals with lipopolysaccharide (LPS) and d-galactosamine (d-GalN)[188].

We set up 4 group of FVB-luc+ mice. 2 groups were injected with d-GalN and and LPS followed by either injection of commercial DEVD-aminoluciferin or combination of our DEVD-(D-Cys) and NH_2-CBT (Fig 5.8). The other two groups were injected with PBS followed by injection of the same imaging reagents as d-GalN/LPS group. The signals from each d-GalN/LPS treated group were compared to each other and their corresponding PBS controls.

The data shown in Fig 5.9 indicate that much stronger signal was produced from the two groups of animals treated with d-GalN/LPS in comparison to the PBS treated group. The ratio in average signal we observed between the d-GalN/LPS-treated and control groups of mice injected with DEVD-aminoluciferin was about 3-fold, which was statistically significant and similar to

the previous report (Fig 5.9A). At the same time, the ratio between the signals produced from d-GalN/LPS-treated and control groups of mice, injected with combination of DEVD-(D-Cys) and NH$_2$-CBT, was about 5.2-fold, higher than that of the commercial DEVD-aminoluciferin substrate. Importantly, this difference was also statistically significant.

Together, these results demonstrate that the combination of DEVD-(D-Cys) and CBTs represents a valuable tool for non-invasive quantification and real-time visualization of caspas3 activity directly in living animals.
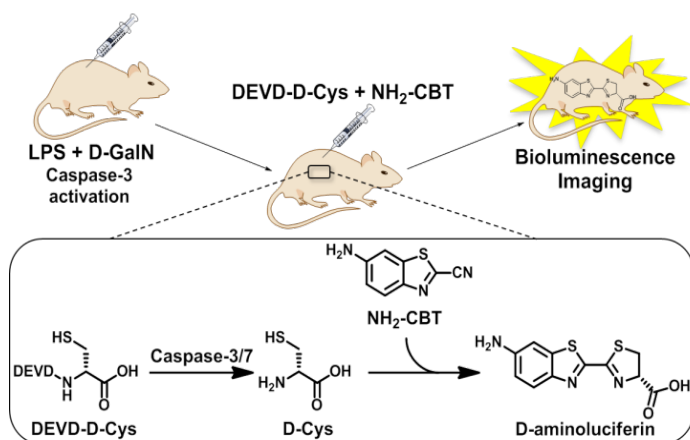
Figure 5.8. Overall representation of caspase-3 activity imaging with DEVD-D-Cys peptide and amino-CBT in living animals.
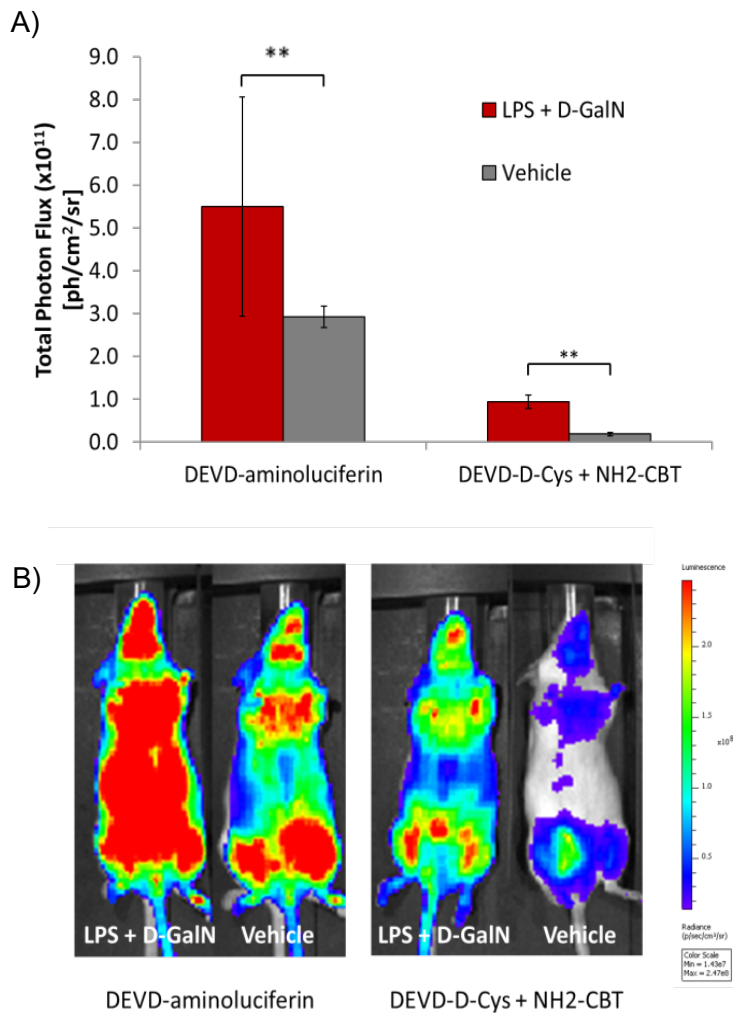
Figure 5.9. Caspase-3 activity imaging using luciferin ligation reaction in living transgenic reporter mice.
A) Total photon flux integrated over 1 hr that was obtained from transgenic reporter mice treated with either PBS or combination of LPS and D-GalN. Six hours post treatment, the animals received IP injections of either DEVD-aminoluciferin or combination of DEVD-D-Cys peptide and amino-CBT. Statistical analyses were performed with a two-tailed Student's t test. **$P < 0.01$ (n=4) and error bars are ± SD for four measurements. B) Representative image of mice, 15 min post-injection of DEVD-aminoluciferin or combination treatment with DEVD-D-Cys and amino-CBT reagents. Statistical analyses were performed with a two-tailed Student's t test. **$P < 0.01$ (n=4) and error bars are ± SD for four measurements.

Conclusion

In this study we demonstrated that CBTs and D-cysteine could efficiently react with each other in live animals and cells. This particular feature allows this reaction to be extremely valuable for complex biological processes studies especially in live mice mainly because only the Staudinger ligation has been show to work efficiently[159, 161]. Additionally, the split luciferin ligation reaction contains several other unique features such as easy manipulation that make it very useful for a vast range of exciting biological applications.

Moreover, the chemistry of the reagents involved in the new in vivo reaction is fitting for the development of novel applications. One of which is the direct real-time imaging of protease activity in living animals. In this report, we show the successful application of real time non-invasive imaging of caspase 3 activity in hepatic apoptosis animal models. In comparison to commercially available DEVD-aminoluciferin substrate, the split luciferin ligation reagents demonstrated a notably higher signal to background ratio, ultimately showing the potential of this new method for sensitive imaging of apoptosis.

Taken together, this novel luciferin ligation reaction is extremely valuable for in vivo imaging and biocompatible labeling strategies and exhibits a lot of potential for the field of preclinical research and chemical biology.
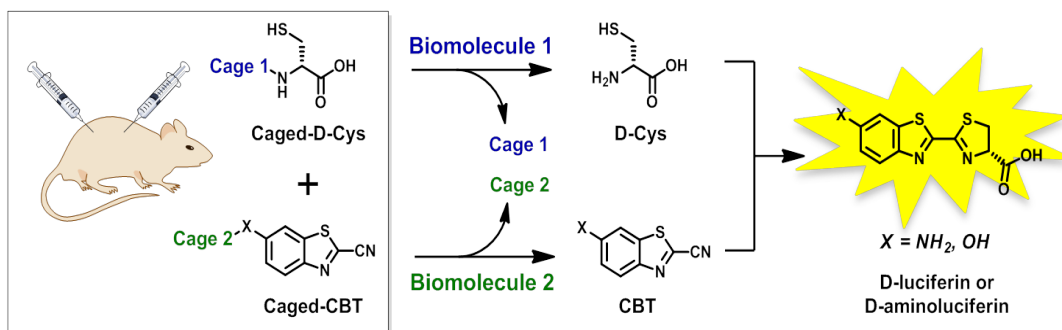
Figure 5.11. Overall representation of dual imaging concept for luciferin ligation

Both luciferin ligation precursors could caged as a sensors for two different biomolecules. Only when both become uncaged free D-luciferin or D-aminoluciferin is formed followed by production of light.

References

1.	Contag CH. In vivo pathology: seeing with molecular specificity and cellular resolution in the living body. Annu Rev Pathol 2007;2:277-305.
2.	Baker M. Whole-animal imaging: The whole picture. Nature 2010;463:977-80.
3.	Contag CH, Bachmann MH. Advances in in vivo bioluminescence imaging of gene expression. Annu Rev Biomed Eng 2002;4:235-60.
4.	Greer LF, 3rd, Szalay AA. Imaging of light emission from the expression of luciferases in living cells and organisms: a review. Luminescence 2002;17:43-74.
5.	Ruby EG, Lee KH. The Vibrio fischeri-Euprymna scolopes Light Organ Association: Current Ecological Paradigms. Appl Environ Microbiol 1998;64:805-12.
6.	Visick KL, McFall-Ngai MJ. An exclusive contract: specificity in the Vibrio fischeri-Euprymna scolopes partnership. J Bacteriol 2000;182:1779-87.
7.	McElroy WD, Seliger HH, White EH. Mechanism of bioluminescence, chemiluminescence and enzyme function in the oxidation of firefly luciferin. Photochem Photobiol 1969;10:153-70.
8.	Zhao H, Doyle TC, Coquoz O, et al. Emission spectra of bioluminescent reporters and interaction with mammalian tissue determine the sensitivity of detection in vivo. J Biomed Opt 2005;10:41210.
9.	Contag CH, Spilman SD, Contag PR, et al. Visualizing gene expression in living mammals using a bioluminescent reporter. Photochem Photobiol 1997;66:523-31.
10.	Dothager RS, Flentie K, Moss B, et al. Advances in bioluminescence imaging of live animal models. Curr Opin Biotechnol 2009;20:45-53.
11.	Contag CH, Contag PR, Mullins JI, et al. Photonic detection of bacterial pathogens in living hosts. Mol Microbiol 1995;18:593-603.
12.	Contag PR, Olomu IN, Stevenson DK, et al. Bioluminescent indicators in living mammals. Nat Med 1998;4:245-7.
13.	Close DM, Xu T, Sayler GS, et al. In vivo bioluminescent imaging (BLI): noninvasive visualization and interrogation of biological processes in living animals. Sensors (Basel) 2011;11:180-206.
14.	Mandl S, Schimmelpfennig C, Edinger M, et al. Understanding immune cell trafficking patterns via in vivo bioluminescence imaging. J Cell Biochem Suppl 2002;39:239-48.
15.	Edinger M, Sweeney TJ, Tucker AA, et al. Noninvasive assessment of tumor cell proliferation in animal models. Neoplasia 1999;1:303-10.
16.	Adams JY, Johnson M, Sato M, et al. Visualization of advanced human prostate cancer lesions in living mice by a targeted gene transfer vector and optical imaging. Nat Med 2002;8:891-7.

17. Wetterwald A, van der Pluijm G, Que I, et al. Optical imaging of cancer metastasis to bone marrow: a mouse model of minimal residual disease. Am J Pathol 2002;160:1143-53.
18. van der Bogt KE, Hellingman AA, Lijkwan MA, et al. Molecular imaging of bone marrow mononuclear cell survival and homing in murine peripheral artery disease. JACC Cardiovasc Imaging 2012;5:46-55.
19. Wu JC, Chen IY, Sundaresan G, et al. Molecular imaging of cardiac cell transplantation in living animals using optical bioluminescence and positron emission tomography. Circulation 2003;108:1302-5.
20. Hardy J, Edinger M, Bachmann MH, et al. Bioluminescence imaging of lymphocyte trafficking in vivo. Exp Hematol 2001;29:1353-60.
21. Bernau K, Lewis CM, Petelinsek AM, et al. In vivo tracking of human neural progenitor cells in the rat brain using bioluminescence imaging. J Neurosci Methods 2014;228:67-78.
22. Rabinovich BA, Ye Y, Etto T, et al. Visualizing fewer than 10 mouse T cells with an enhanced firefly luciferase in immunocompetent mouse models of cancer. Proc Natl Acad Sci U S A 2008;105:14342-6.
23. Santos EB, Yeh R, Lee J, et al. Sensitive in vivo imaging of T cells using a membrane-bound Gaussia princeps luciferase. Nat Med 2009;15:338-44.
24. Prescher JA, Contag CH. Guided by the light: visualizing biomolecular processes in living animals with bioluminescence. Curr Opin Chem Biol 2010;14:80-9.
25. Malstrom SE, Jekic-McMullen D, Sambucetti L, et al. In vivo bioluminescent monitoring of chemical toxicity using heme oxygenase-luciferase transgenic mice. Toxicol Appl Pharmacol 2004;200:219-28.
26. Lehmann S, Stiehl DP, Honer M, et al. Longitudinal and multimodal in vivo imaging of tumor hypoxia and its downstream molecular events. Proc Natl Acad Sci U S A 2009;106:14004-9.
27. Liu AC, Welsh DK, Ko CH, et al. Intercellular coupling confers robustness against mutations in the SCN circadian clock network. Cell 2007;129:605-16.
28. O'Connell-Rodwell CE, Mackanos MA, Simanovskii D, et al. In vivo analysis of heat-shock-protein-70 induction following pulsed laser irradiation in a transgenic reporter mouse. J Biomed Opt 2008;13:030501.
29. Ishikawa TO, Jain NK, Taketo MM, et al. Imaging cyclooxygenase-2 (Cox-2) gene expression in living animals with a luciferase knock-in reporter gene. Mol Imaging Biol 2006;8:171-87.
30. Keller AF, Gravel M, Kriz J. Live imaging of amyotrophic lateral sclerosis pathogenesis: disease onset is characterized by marked induction of GFAP in Schwann cells. Glia 2009;57:1130-42.

31. Luo J, Lin AH, Masliah E, et al. Bioluminescence imaging of Smad signaling in living mice shows correlation with excitotoxic neurodegeneration. Proc Natl Acad Sci U S A 2006;103:18326-31.
32. Moroz E, Carlin S, Dyomina K, et al. Real-time imaging of HIF-1alpha stabilization and degradation. PLoS One 2009;4:e5077.
33. Cohen AS, Dubikovskaya EA, Rush JS, et al. Real-time bioluminescence imaging of glycans on live cells. J Am Chem Soc 2010;132:8563-5.
34. Van de Bittner GC, Bertozzi CR, Chang CJ. Strategy for dual-analyte luciferin imaging: in vivo bioluminescence detection of hydrogen peroxide and caspase activity in a murine model of acute inflammation. J Am Chem Soc 2013;135:1783-95.
35. Wehrman TS, von Degenfeld G, Krutzik PO, et al. Luminescent imaging of beta-galactosidase activity in living subjects using sequential reporter-enzyme luminescence. Nat Methods 2006;3:295-301.
36. Hickson J, Ackler S, Klaubert D, et al. Noninvasive molecular imaging of apoptosis in vivo using a modified firefly luciferase substrate, Z-DEVD-aminoluciferin. Cell Death Differ 2010;17:1003-10.
37. Scabini M, Stellari F, Cappella P, et al. In vivo imaging of early stage apoptosis by measuring real-time caspase-3/7 activation. Apoptosis 2011;16:198-207.
38. Shah K, Tung CH, Breakefield XO, et al. In vivo imaging of S-TRAIL-mediated tumor regression and apoptosis. Mol Ther 2005;11:926-31.
39. Dragulescu-Andrasi A, Liang G, Rao J. In vivo bioluminescence imaging of furin activity in breast cancer cells using bioluminogenic substrates. Bioconjug Chem 2009;20:1660-6.
40. Yao H, So MK, Rao J. A bioluminogenic substrate for in vivo imaging of beta-lactamase activity. Angew Chem Int Ed Engl 2007;46:7031-4.
41. Laxman B, Hall DE, Bhojani MS, et al. Noninvasive real-time imaging of apoptosis. Proc Natl Acad Sci U S A 2002;99:16551-5.
42. Henkin AH, Cohen AS, Dubikovskaya EA, et al. Real-time noninvasive imaging of fatty acid uptake in vivo. ACS Chem Biol 2012;7:1884-91.
43. Van de Bittner GC, Dubikovskaya EA, Bertozzi CR, et al. In vivo imaging of hydrogen peroxide production in a murine tumor model with a chemoselective bioluminescent reporter. Proc Natl Acad Sci U S A 2010;107:21316-21.
44. el-Serag HB. Epidemiology of hepatocellular carcinoma. Clin Liver Dis 2001;5:87-107, vi.
45. Ferlay J, Soerjomataram I, Dikshit R, et al. Cancer incidence and mortality worldwide: sources, methods and major patterns in GLOBOCAN 2012. Int J Cancer 2015;136:E359-86.
46. Eggert T, McGlynn KA, Duffy A, et al. Epidemiology of fibrolamellar hepatocellular carcinoma in the USA, 2000-10. Gut 2013;62:1667-8.

47. Riggle KM, Turnham R, Scott JD, et al. Fibrolamellar Hepatocellular Carcinoma: Mechanistic Distinction From Adult Hepatocellular Carcinoma. Pediatr Blood Cancer 2016;63:1163-7.

48. Zhu YP, Chen YM, Matro E, et al. Primary hepatic angiosarcoma: A report of two cases and literature review. World J Gastroenterol 2015;21:6088-96.

49. Patel T. Increasing incidence and mortality of primary intrahepatic cholangiocarcinoma in the United States. Hepatology 2001;33:1353-7.

50. Shaib YH, Davila JA, McGlynn K, et al. Rising incidence of intrahepatic cholangiocarcinoma in the United States: a true increase? J Hepatol 2004;40:472-7.

51. He L, Tian DA, Li PY, et al. Mouse models of liver cancer: Progress and recommendations. Oncotarget 2015;6:23306-22.

52. Verna L, Whysner J, Williams GM. N-nitrosodiethylamine mechanistic data and risk assessment: bioactivation, DNA-adduct formation, mutagenicity, and tumor initiation. Pharmacol Ther 1996;71:57-81.

53. Chakraborty T, Chatterjee A, Rana A, et al. Carcinogen-induced early molecular events and its implication in the initiation of chemical hepatocarcinogenesis in rats: chemopreventive role of vanadium on this process. Biochim Biophys Acta 2007;1772:48-59.

54. Kaina B, Christmann M, Naumann S, et al. MGMT: key node in the battle against genotoxicity, carcinogenicity and apoptosis induced by alkylating agents. DNA Repair (Amst) 2007;6:1079-99.

55. Hacker HJ, Mtiro H, Bannasch P, et al. Histochemical profile of mouse hepatocellular adenomas and carcinomas induced by a single dose of diethylnitrosamine. Cancer Res 1991;51:1952-8.

56. Park TJ, Kim JY, Oh SP, et al. TIS21 negatively regulates hepatocarcinogenesis by disruption of cyclin B1-Forkhead box M1 regulation loop. Hepatology 2008;47:1533-43.

57. Lee GH. Paradoxical effects of phenobarbital on mouse hepatocarcinogenesis. Toxicol Pathol 2000;28:215-25.

58. Anisimov VN, Ukraintseva SV, Yashin AI. Cancer in rodents: does it tell us about cancer in humans? Nat Rev Cancer 2005;5:807-19.

59. Vesselinovitch SD, Mihailovich N. Kinetics of diethylnitrosamine hepatocarcinogenesis in the infant mouse. Cancer Res 1983;43:4253-9.

60. Goldfarb S, Pugh TD, Kosciuk S, et al. Kinetics of diethylnitrosamine hepatocarcinogenesis in the infant mouse. Cancer Res 1985;45:909-12.

61. Bagi CM, Andresen CJ. Models of hepatocellular carcinoma and biomarker strategy. Cancers (Basel) 2010;2:1441-52.

62. Leenders MW, Nijkamp MW, Borel Rinkes IH. Mouse models in liver cancer research: a review of current literature. World J Gastroenterol 2008;14:6915-23.

63. Rygaard J, Povlsen CO. Heterotransplantation of a human malignant tumour to "Nude" mice. Acta Pathol Microbiol Scand 1969;77:758-60.

64. Cany J, Tran L, Gauttier V, et al. Immunotherapy of hepatocellular carcinoma: is there a place for regulatory T-lymphocyte depletion? Immunotherapy 2011;3:32-4.

65. Heijstek MW, Kranenburg O, Borel Rinkes IH. Mouse models of colorectal cancer and liver metastases. Dig Surg 2005;22:16-25.

66. Killion JJ, Radinsky R, Fidler IJ. Orthotopic models are necessary to predict therapy of transplantable tumors in mice. Cancer Metastasis Rev 1998;17:279-84.

67. Bibby MC. Orthotopic models of cancer for preclinical drug evaluation: advantages and disadvantages. Eur J Cancer 2004;40:852-7.

68. Khanna C, Hunter K. Modeling metastasis in vivo. Carcinogenesis 2005;26:513-23.

69. Troiani T, Schettino C, Martinelli E, et al. The use of xenograft models for the selection of cancer treatments with the EGFR as an example. Crit Rev Oncol Hematol 2008;65:200-11.

70. Imbeaud S, Ladeiro Y, Zucman-Rossi J. Identification of novel oncogenes and tumor suppressors in hepatocellular carcinoma. Semin Liver Dis 2010;30:75-86.

71. Zender L, Villanueva A, Tovar V, et al. Cancer gene discovery in hepatocellular carcinoma. J Hepatol 2010;52:921-9.

72. Heindryckx F, Colle I, Van Vlierberghe H. Experimental mouse models for hepatocellular carcinoma research. Int J Exp Pathol 2009;90:367-86.

73. Newell P, Villanueva A, Friedman SL, et al. Experimental models of hepatocellular carcinoma. J Hepatol 2008;48:858-79.

74. Buendia MA. Genetics of hepatocellular carcinoma. Semin Cancer Biol 2000;10:185-200.

75. Colnot S, Decaens T, Niwa-Kawakita M, et al. Liver-targeted disruption of Apc in mice activates beta-catenin signaling and leads to hepatocellular carcinomas. Proc Natl Acad Sci U S A 2004;101:17216-21.

76. Ahuja D, Saenz-Robles MT, Pipas JM. SV40 large T antigen targets multiple cellular pathways to elicit cellular transformation. Oncogene 2005;24:7729-45.

77. Ali SH, DeCaprio JA. Cellular transformation by SV40 large T antigen: interaction with host proteins. Semin Cancer Biol 2001;11:15-23.

78. Kim CM, Koike K, Saito I, et al. HBx gene of hepatitis B virus induces liver cancer in transgenic mice. Nature 1991;351:317-20.

79. Moriya K, Fujie H, Shintani Y, et al. The core protein of hepatitis C virus induces hepatocellular carcinoma in transgenic mice. Nat Med 1998;4:1065-7.

80. Richmond A, Su Y. Mouse xenograft models vs GEM models for human cancer therapeutics. Dis Model Mech 2008;1:78-82.
81. Harada H, Kizaka-Kondoh S, Li G, et al. Significance of HIF-1-active cells in angiogenesis and radioresistance. Oncogene 2007;26:7508-16.
82. Liu F, Song Y, Liu D. Hydrodynamics-based transfection in animals by systemic administration of plasmid DNA. Gene Ther 1999;6:1258-66.
83. Zhang G, Budker V, Wolff JA. High levels of foreign gene expression in hepatocytes after tail vein injections of naked plasmid DNA. Hum Gene Ther 1999;10:1735-7.
84. Chen X, Calvisi DF. Hydrodynamic transfection for generation of novel mouse models for liver cancer research. Am J Pathol 2014;184:912-23.
85. Ivics Z, Hackett PB, Plasterk RH, et al. Molecular reconstruction of Sleeping Beauty, a Tc1-like transposon from fish, and its transposition in human cells. Cell 1997;91:501-10.
86. Mikkelsen JG, Yant SR, Meuse L, et al. Helper-Independent Sleeping Beauty transposon-transposase vectors for efficient nonviral gene delivery and persistent gene expression in vivo. Mol Ther 2003;8:654-65.
87. Yant SR, Meuse L, Chiu W, et al. Somatic integration and long-term transgene expression in normal and haemophilic mice using a DNA transposon system. Nat Genet 2000;25:35-41.
88. Ho C, Wang C, Mattu S, et al. AKT (v-akt murine thymoma viral oncogene homolog 1) and N-Ras (neuroblastoma ras viral oncogene homolog) coactivation in the mouse liver promotes rapid carcinogenesis by way of mTOR (mammalian target of rapamycin complex 1), FOXM1 (forkhead box M1)/SKP2, and c-Myc pathways. Hepatology 2012;55:833-45.
89. Stauffer JK, Scarzello AJ, Andersen JB, et al. Coactivation of AKT and beta-catenin in mice rapidly induces formation of lipogenic liver tumors. Cancer Res 2011;71:2718-27.
90. Farazi PA, Zeisberg M, Glickman J, et al. Chronic bile duct injury associated with fibrotic matrix microenvironment provokes cholangiocarcinoma in p53-deficient mice. Cancer Res 2006;66:6622-7.
91. Johnson JI, Decker S, Zaharevitz D, et al. Relationships between drug activity in NCI preclinical in vitro and in vivo models and early clinical trials. Br J Cancer 2001;84:1424-31.
92. Sausville EA, Burger AM. Contributions of human tumor xenografts to anticancer drug development. Cancer Res 2006;66:3351-4, discussion 3354.
93. Voskoglou-Nomikos T, Pater JL, Seymour L. Clinical predictive value of the in vitro cell line, human xenograft, and mouse allograft preclinical cancer models. Clin Cancer Res 2003;9:4227-39.
94. Fan B, Malato Y, Calvisi DF, et al. Cholangiocarcinomas can originate from hepatocytes in mice. J Clin Invest 2012;122:2911-5.

95. Evert M, Dombrowski F, Fan B, et al. On the role of notch1 and adult hepatocytes in murine intrahepatic cholangiocarcinoma development. Hepatology 2013;58:1857-9.

96. Fabbrini E, Sullivan S, Klein S. Obesity and nonalcoholic fatty liver disease: biochemical, metabolic, and clinical implications. Hepatology 2010;51:679-89.

97. Karpe F, Dickmann JR, Frayn KN. Fatty acids, obesity, and insulin resistance: time for a reevaluation. Diabetes 2011;60:2441-9.

98. Koonen DP, Jacobs RL, Febbraio M, et al. Increased hepatic CD36 expression contributes to dyslipidemia associated with diet-induced obesity. Diabetes 2007;56:2863-71.

99. Hauner H. The mode of action of thiazolidinediones. Diabetes Metab Res Rev 2002;18 Suppl 2:S10-5.

100. Kawaguchi K, Sakaida I, Tsuchiya M, et al. Pioglitazone prevents hepatic steatosis, fibrosis, and enzyme-altered lesions in rat liver cirrhosis induced by a choline-deficient L-amino acid-defined diet. Biochem Biophys Res Commun 2004;315:187-95.

101. Yoshinaga K, Tamaki N. Imaging myocardial metabolism. Curr Opin Biotechnol 2007;18:52-9.

102. DeGrado TR, Wang S, Holden JE, et al. Synthesis and preliminary evaluation of (18)F-labeled 4-thia palmitate as a PET tracer of myocardial fatty acid oxidation. Nucl Med Biol 2000;27:221-31.

103. Peterson LR, Gropler RJ. Radionuclide imaging of myocardial metabolism. Circ Cardiovasc Imaging 2010;3:211-22.

104. Nie B, Park HM, Kazantzis M, et al. Specific bile acids inhibit hepatic fatty acid uptake in mice. Hepatology 2012;56:1300-10.

105. Oosterveer MH, Grefhorst A, van Dijk TH, et al. Fenofibrate simultaneously induces hepatic fatty acid oxidation, synthesis, and elongation in mice. J Biol Chem 2009;284:34036-44.

106. Ferrell JM, Chiang JY. Circadian rhythms in liver metabolism and disease. Acta Pharm Sin B 2015;5:113-22.

107. Kohsaka A, Laposky AD, Ramsey KM, et al. High-fat diet disrupts behavioral and molecular circadian rhythms in mice. Cell Metab 2007;6:414-21.

108. Patel VR, Eckel-Mahan K, Sassone-Corsi P, et al. CircadiOmics: integrating circadian genomics, transcriptomics, proteomics and metabolomics. Nat Methods 2012;9:772-3.

109. Shaib Y, El-Serag HB. The epidemiology of cholangiocarcinoma. Semin Liver Dis 2004;24:115-25.

110. Khan SA, Emadossadaty S, Ladep NG, et al. Rising trends in cholangiocarcinoma: is the ICD classification system misleading us? J Hepatol 2012;56:848-54.

111. Plentz RR, Malek NP. Clinical presentation, risk factors and staging systems of cholangiocarcinoma. Best Pract Res Clin Gastroenterol 2015;29:245-52.
112. Thinkhamrop K, Khuntikeo N, Phonjitt P, et al. Association between Diabetes Mellitus and Fatty Liver Based on Ultrasonography Screening in the World's Highest Cholangiocarcinoma Incidence Region, Northeast Thailand. Asian Pac J Cancer Prev 2015;16:3931-6.
113. Yoshida GJ. Metabolic reprogramming: the emerging concept and associated therapeutic strategies. J Exp Clin Cancer Res 2015;34:111.
114. Currie E, Schulze A, Zechner R, et al. Cellular fatty acid metabolism and cancer. Cell Metab 2013;18:153-61.
115. Santos CR, Schulze A. Lipid metabolism in cancer. FEBS J 2012;279:2610-23.
116. Flavin R, Peluso S, Nguyen PL, et al. Fatty acid synthase as a potential therapeutic target in cancer. Future Oncol 2010;6:551-62.
117. Menendez JA, Lupu R. Fatty acid synthase and the lipogenic phenotype in cancer pathogenesis. Nat Rev Cancer 2007;7:763-77.
118. Mullen GE, Yet L. Progress in the development of fatty acid synthase inhibitors as anticancer targets. Bioorg Med Chem Lett 2015;25:4363-9.
119. Ros S, Santos CR, Moco S, et al. Functional metabolic screen identifies 6-phosphofructo-2-kinase/fructose-2,6-biphosphatase 4 as an important regulator of prostate cancer cell survival. Cancer Discov 2012;2:328-43.
120. De Pergola G, Silvestris F. Obesity as a major risk factor for cancer. J Obes 2013;2013:291546.
121. Vucenik I, Stains JP. Obesity and cancer risk: evidence, mechanisms, and recommendations. Ann N Y Acad Sci 2012;1271:37-43.
122. Li L, Che L, Tharp KM, et al. Differential requirement for de novo lipogenesis in cholangiocarcinoma and hepatocellular carcinoma of mice and humans. Hepatology 2016;63:1900-13.
123. Doege H, Stahl A. Protein-mediated fatty acid uptake: novel insights from in vivo models. Physiology (Bethesda) 2006;21:259-68.
124. Anderson CM, Stahl A. SLC27 fatty acid transport proteins. Mol Aspects Med 2013;34:516-28.
125. Kazantzis M, Stahl A. Fatty acid transport proteins, implications in physiology and disease. Biochim Biophys Acta 2012;1821:852-7.
126. Falcon A, Doege H, Fluitt A, et al. FATP2 is a hepatic fatty acid transporter and peroxisomal very long-chain acyl-CoA synthetase. Am J Physiol Endocrinol Metab 2010.
127. Doege H, Grimm D, Falcon A, et al. Silencing of hepatic fatty acid transporter protein 5 in vivo reverses diet-induced non-alcoholic fatty liver disease and improves hyperglycemia. J Biol Chem 2008;283:22186-92.

128. Falcon A, Doege H, Fluitt A, et al. FATP2 is a hepatic fatty acid transporter and peroxisomal very long-chain acyl-CoA synthetase. Am J Physiol Endocrinol Metab 2010;299:E384-93.
129. Zhang G, Gao X, Song YK, et al. Hydroporation as the mechanism of hydrodynamic delivery. Gene Ther 2004;11:675-82.
130. Doege H, Baillie RA, Ortegon AM, et al. Targeted deletion of FATP5 reveals multiple functions in liver metabolism: alterations in hepatic lipid homeostasis. Gastroenterology 2006;130:1245-58.
131. Li L, Pilo GM, Li X, et al. Inactivation of fatty acid synthase impairs hepatocarcinogenesis driven by AKT in mice and humans. J Hepatol 2016;64:333-41.
132. McCord JM, Fridovich I. Superoxide dismutase. An enzymic function for erythrocuprein (hemocuprein). J Biol Chem 1969;244:6049-55.
133. Reddi AR, Culotta VC. SOD1 integrates signals from oxygen and glucose to repress respiration. Cell 2013;152:224-35.
134. Ferguson-Miller S, Babcock GT. Heme/Copper Terminal Oxidases. Chem Rev 1996;96:2889-2908.
135. Ishida S, Andreux P, Poitry-Yamate C, et al. Bioavailable copper modulates oxidative phosphorylation and growth of tumors. Proc Natl Acad Sci U S A 2013;110:19507-12.
136. Brady DC, Crowe MS, Turski ML, et al. Copper is required for oncogenic BRAF signalling and tumorigenesis. Nature 2014;509:492-6.
137. Chang CJ. Searching for harmony in transition-metal signaling. Nat Chem Biol 2015;11:744-7.
138. Dodani SC, Firl A, Chan J, et al. Copper is an endogenous modulator of neural circuit spontaneous activity. Proc Natl Acad Sci U S A 2014;111:16280-5.
139. Turski ML, Brady DC, Kim HJ, et al. A novel role for copper in Ras/mitogen-activated protein kinase signaling. Mol Cell Biol 2012;32:1284-95.
140. Aron AT, Ramos-Torres KM, Cotruvo JA, Jr., et al. Recognition- and reactivity-based fluorescent probes for studying transition metal signaling in living systems. Acc Chem Res 2015;48:2434-42.
141. Camakaris J, Voskoboinik I, Mercer JF. Molecular mechanisms of copper homeostasis. Biochem Biophys Res Commun 1999;261:225-32.
142. Kaler SG. ATP7A-related copper transport diseases-emerging concepts and future trends. Nat Rev Neurol 2011;7:15-29.
143. Puig S, Thiele DJ. Molecular mechanisms of copper uptake and distribution. Curr Opin Chem Biol 2002;6:171-80.
144. Desai V, Kaler SG. Role of copper in human neurological disorders. Am J Clin Nutr 2008;88:855S-8S.

145. Huster D, Lutsenko S. Wilson disease: not just a copper disorder. Analysis of a Wilson disease model demonstrates the link between copper and lipid metabolism. Mol Biosyst 2007;3:816-24.
146. Aigner E, Strasser M, Haufe H, et al. A role for low hepatic copper concentrations in nonalcoholic Fatty liver disease. Am J Gastroenterol 2010;105:1978-85.
147. Aigner E, Theurl I, Haufe H, et al. Copper availability contributes to iron perturbations in human nonalcoholic fatty liver disease. Gastroenterology 2008;135:680-8.
148. Carr TP, Lei KY. High-density lipoprotein cholesteryl ester and protein catabolism in hypercholesterolemic rats induced by copper deficiency. Metabolism 1990;39:518-24.
149. Feldman A, Aigner E, Weghuber D, et al. The Potential Role of Iron and Copper in Pediatric Obesity and Nonalcoholic Fatty Liver Disease. Biomed Res Int 2015;2015:287401.
150. Gong D, Lu J, Chen X, et al. A copper(II)-selective chelator ameliorates diabetes-evoked renal fibrosis and albuminuria, and suppresses pathogenic TGF-beta activation in the kidneys of rats used as a model of diabetes. Diabetologia 2008;51:1741-51.
151. Stattermayer AF, Traussnigg S, Dienes HP, et al. Hepatic steatosis in Wilson disease--Role of copper and PNPLA3 mutations. J Hepatol 2015;63:156-63.
152. Cotruvo JA, Jr., Aron AT, Ramos-Torres KM, et al. Synthetic fluorescent probes for studying copper in biological systems. Chem Soc Rev 2015;44:4400-14.
153. Hirayama T, Van de Bittner GC, Gray LW, et al. Near-infrared fluorescent sensor for in vivo copper imaging in a murine Wilson disease model. Proc Natl Acad Sci U S A 2012;109:2228-33.
154. Li J, Chen L, Du L, et al. Cage the firefly luciferin! - a strategy for developing bioluminescent probes. Chem Soc Rev 2013;42:662-76.
155. Taki M, Iyoshi S, Ojida A, et al. Development of highly sensitive fluorescent probes for detection of intracellular copper(I) in living systems. J Am Chem Soc 2010;132:5938-9.
156. Kobayashi M, Shimizu S. Cobalt proteins. Eur J Biochem 1999;261:1-9.
157. Aigner E, Weiss G, Datz C. Dysregulation of iron and copper homeostasis in nonalcoholic fatty liver. World J Hepatol 2015;7:177-88.
158. Church SJ, Begley P, Kureishy N, et al. Deficient copper concentrations in dried-defatted hepatic tissue from ob/ob mice: A potential model for study of defective copper regulation in metabolic liver disease. Biochem Biophys Res Commun 2015;460:549-54.
159. Sletten EM, Bertozzi CR. Bioorthogonal chemistry: fishing for selectivity in a sea of functionality. Angew Chem Int Ed Engl 2009;48:6974-98.

160. Agard NJ, Baskin JM, Prescher JA, et al. A comparative study of bioorthogonal reactions with azides. ACS Chem Biol 2006;1:644-8.
161. Chang PV, Prescher JA, Sletten EM, et al. Copper-free click chemistry in living animals. Proc Natl Acad Sci U S A 2010;107:1821-6.
162. Ning X, Guo J, Wolfert MA, et al. Visualizing metabolically labeled glycoconjugates of living cells by copper-free and fast huisgen cycloadditions. Angew Chem Int Ed Engl 2008;47:2253-5.
163. Hangauer MJ, Bertozzi CR. A FRET-based fluorogenic phosphine for live-cell imaging with the Staudinger ligation. Angew Chem Int Ed Engl 2008;47:2394-7.
164. Nilsson BL, Kiessling LL, Raines RT. Staudinger ligation: a peptide from a thioester and azide. Org Lett 2000;2:1939-41.
165. Saxon E, Armstrong JI, Bertozzi CR. A "traceless" Staudinger ligation for the chemoselective synthesis of amide bonds. Org Lett 2000;2:2141-3.
166. Devaraj NK, Weissleder R, Hilderbrand SA. Tetrazine-based cycloadditions: application to pretargeted live cell imaging. Bioconjug Chem 2008;19:2297-9.
167. Lang K, Davis L, Wallace S, et al. Genetic Encoding of bicyclononynes and trans-cyclooctenes for site-specific protein labeling in vitro and in live mammalian cells via rapid fluorogenic Diels-Alder reactions. J Am Chem Soc 2012;134:10317-20.
168. Rogers AB. Gastric Helicobacter spp. in animal models: pathogenesis and modulation by extragastric coinfections. Methods Mol Biol 2012;921:175-88.
169. Yang J, Seckute J, Cole CM, et al. Live-cell imaging of cyclopropene tags with fluorogenic tetrazine cycloadditions. Angew Chem Int Ed Engl 2012;51:7476-9.
170. Wiley RA, Sternson LA, Sasame HA, et al. Enzymatic oxidation of diphenylmethylphosphine and 3-dimethylaminopropyldiphenylphosphine by rat liver microsomes. Biochem Pharmacol 1972;21:3235-47.
171. Lin FL, Hoyt HM, van Halbeek H, et al. Mechanistic investigation of the staudinger ligation. J Am Chem Soc 2005;127:2686-95.
172. White EH, Rapaport E, Hopkins TA, et al. Chemi- and bioluminescence of firefly luciferin. J Am Chem Soc 1969;91:2178-80.
173. Liang G, Ren H, Rao J. A biocompatible condensation reaction for controlled assembly of nanostructures in living cells. Nat Chem 2010;2:54-60.
174. Nguyen DP, Elliott T, Holt M, et al. Genetically encoded 1,2-aminothiols facilitate rapid and site-specific protein labeling via a bio-orthogonal cyanobenzothiazole condensation. J Am Chem Soc 2011;133:11418-21.

175. Ren H, Xiao F, Zhan K, et al. A biocompatible condensation reaction for the labeling of terminal cysteine residues on proteins. Angew Chem Int Ed Engl 2009;48:9658-62.
176. Ye D, Liang G, Ma ML, et al. Controlling intracellular macrocyclization for the imaging of protease activity. Angew Chem Int Ed Engl 2011;50:2275-9.
177. Goun EA, Pillow TH, Jones LR, et al. Molecular transporters: synthesis of oligoguanidinium transporters and their application to drug delivery and real-time imaging. Chembiochem 2006;7:1497-515.
178. Jones LR, Goun EA, Shinde R, et al. Releasable luciferin-transporter conjugates: tools for the real-time analysis of cellular uptake and release. J Am Chem Soc 2006;128:6526-7.
179. O'Brien MA, Daily WJ, Hesselberth PE, et al. Homogeneous, bioluminescent protease assays: caspase-3 as a model. J Biomol Screen 2005;10:137-48.
180. Woodroofe CC, Shultz JW, Wood MG, et al. N-Alkylated 6'-aminoluciferins are bioluminescent substrates for Ultra-Glo and QuantiLum luciferase: new potential scaffolds for bioluminescent assays. Biochemistry 2008;47:10383-93.
181. Harwood KR, Mofford DM, Reddy GR, et al. Identification of mutant firefly luciferases that efficiently utilize aminoluciferins. Chem Biol 2011;18:1649-57.
182. Reddy GR, Thompson WC, Miller SC. Robust light emission from cyclic alkylaminoluciferin substrates for firefly luciferase. J Am Chem Soc 2010;132:13586-7.
183. Gross S, Piwnica-Worms D. Spying on cancer: molecular imaging in vivo with genetically encoded reporters. Cancer Cell 2005;7:5-15.
184. Jurisicova A, Antenos M, Varmuza S, et al. Expression of apoptosis-related genes during human preimplantation embryo development: potential roles for the Harakiri gene product and Caspase-3 in blastomere fragmentation. Mol Hum Reprod 2003;9:133-41.
185. Lakhani SA, Masud A, Kuida K, et al. Caspases 3 and 7: key mediators of mitochondrial events of apoptosis. Science 2006;311:847-51.
186. Shin S, Sung BJ, Cho YS, et al. An anti-apoptotic protein human survivin is a direct inhibitor of caspase-3 and -7. Biochemistry 2001;40:1117-23.
187. Talanian RV, Quinlan C, Trautz S, et al. Substrate specificities of caspase family proteases. J Biol Chem 1997;272:9677-82.
188. Mignon A, Rouquet N, Fabre M, et al. LPS challenge in D-galactosamine-sensitized mice accounts for caspase-dependent fulminant hepatitis, not for septic shock. Am J Respir Crit Care Med 1999;159:1308-15.

189.   Calvisi DF, Wang C, Ho C, et al. Increased lipogenesis, induced by AKT-mTORC1-RPS6 signaling, promotes development of human hepatocellular carcinoma. Gastroenterology 2011;140:1071-83.

190.   Grimm D, Kern A, Rittner K, et al. Novel tools for production and purification of recombinant adenoassociated virus vectors. Hum Gene Ther 1998;9:2745-60.

191.   Zolotukhin S, Byrne BJ, Mason E, et al. Recombinant adeno-associated virus purification using novel methods improves infectious titer and yield. Gene Ther 1999;6:973-85.

192.   Stennicke HR, Salvesen GS. Caspases: preparation and characterization. Methods 1999;17:313-9.

Appendix: Materials and Methods

<u>**Chapter2**</u>
Animal models.
FVB-Luc[+] (FVB-Tg(CAG-luc,-GFP)L2G85Chco/J) mice were obtained from our in-house breeding colony. Mice were maintained at the 12-h light/12-h dark cycle at 22°C and had free access to food and water. To generate a mouse strain with liver-specific luciferase expression (L-Luc mice), mice bearing the Gt(ROSA)26Sor[tm1(Luc)Kael] allele and Tg(Alb-cre)21Mgn mice were purchased from Jackson Laboratories (stocks 005125 and 003574, respectively) and crossed. Gray-fur mice were bred several times to generate white-fur litters. To examine the effect of fenofibrate, mice were fed a standard laboratory chow diet with or without fenofibrate (0.2% w/w) for 10 days, while having free access to drinking water. All animal studies were approved by and performed according to the guidelines of the Animal Care and Use Committee of the University of California, Berkeley.

General animal imaging methods and data analysis.
A Xenogen IVIS Spectrum instrument (Caliper Life Sciences) was used to obtain luminescence images in all animal experiments. Image analysis was performed using the IVIS Living Image software. Total photon flux in each mouse was determined by drawing a region of interest in the animal and integrating photon flux over the total imaging period. Mice were anesthetized prior to injection and during imaging by isoflurane inhalation.

Intraperitoneal injection of FFA-Luc and luciferin.
Anesthetized mice were intraperitoneally (IP) injected with 100μL of 200μM FFA-Luc in 0.1% (w/v) BSA-containing PBS or with 100μL of 2 mM luciferin in PBS immediately before imaging. Luminescence images were acquired by auto exposure back to back for 50 min in case of FFA-Luc and 25 min in case of luciferin.

Quantification of free luciferin in serum.
Sera were collected before and 10 and 20 min after IP injection of FFA-Luc and luciferin, and 50μl of serum samples was plated on 96-well plates containing reaction solution; firefly luciferase (L9420; Sigma-Aldrich, USA) and ATP (A2383; Sigma-Aldrich, USA) were added immediately before recording the results using a luminometer. Fluorescence signals were measured for 10seconds, and the amount of luciferin was calculated based on a standard curve constructed using a series of luciferin concentrations.

In vivo monitoring of FFA hepatic uptake using fluorescence-labeled FA (BODIPY).

The assay was performed as described previously[104] with minor modifications. In brief, mice fasted overnight were anesthetized with isoflurane and injected IP with DCA (6.4 mg/kg body weight) and then BODIPY (100µl of 2µM solution). After 30 min, mice were euthanized, and livers were harvested and homogenized in RIPA buffer. Liver lysates were prepared with three volumes of Dole's reagent (heptane:2-propanol:2N sulfuric acid = 10:40:1 v/v/v), centrifuged at 18,000 × g for 10 min, and clear organic-phase supernatant (top layer) was collected and added to a 96-well plate for fluorescence measurement.

Diurnal rhythm of FFA hepatic uptake.

Two cohorts of male mice were maintained at a 12-h light/12-h dark cycle; zeitgeber time zero (ZT0) referred to lights on and ZT12 to lights off. The first injection of FFA-Luc was conducted at ZT06 (1 PM) in one group and ZT18 (1AM) in the other, followed by subsequent injections every 30 hours. The signal was measured for 20 min during each imaging and the total photon flux was determined. To avoid light application during dark period assessments, we used night vision goggles and dim red lighting. Serum was collected at the same time points and FFA levels were measured using the FFA kit (Sigma-Aldrich).

Chapter3
Plasmid construction

pCMV/SB, pT3-myr-AKT-HA(Addgene plasmid # 31789) and pT3-EF1a-NICD1 (Addgene plasmid # 46047) were gifts from Xin Chen. The IRES-firefly luciferase coding sequence was amplified from MSCV IRES Luciferase (Addgene plasmid #18760) using the forward primer AATTAGATCTCTCGAGGTTAACGAATTC and backward primer AAAAAGAATTCTTACACGGCGATCTTTCC containing EcoRI restriction site. The product was purified, digested with EcoRI and inserted between the EcoRI sites of pT3-myr-AKT-HA. This construct was named AKT-Luc.

Hydrodynamic trasnfection

Wild-type FVB/N mice were purchased from Jackson Laboratory (CA, UCA). Hydrodynamic injection procedures were conducted as previously described.[189] Briefly, 15 µg of each AKT-Luc and pT3-EF1a-NICD1 constructs and 1.2ug of pCMV/SB constructs(25:1 ratio) were diluted in 2 mL of 0.9% NaCl, filtered, and injected into the lateral tail vein of seven week old mice in 7 to 9 seconds. Injected mice were monitored weekly, and sacrificed at 7 weeks after tumor formation.

AAV vector production

Oligonucleotides against FATP2 and FATP5 were designed as suggested.[127] AAV vector production was carried out in 293T cells and following a previously described calcium phosphate transfection protocol.[190] For analytical large-scale productions, 4 times 10^7 cells were seeded in each of 75-cm flask and the next day transfected with 75µg DNA. AAV vector and helper plasmids were transfected in equimolar amounts. Cells were incubated for 48 h after transfection and then lysed by two consecutive rounds of freeze–thawing, releasing the virus particles into the medium. Vector particles from large preparations were purified and concentrated by iodixanol density centrifugation essentially as described.[191]

Hepatocyte Preparation and fatty acid uptake assays

Mouse livers were cannulated through the portal vein and an incision was made in the inferior vena cava. Liver perfusion with digestion and perfusion media and isolation of hepatocytes was carried out according to the manufacturer's instructions (Gibco, Carlsbad, CA). After isolation, hepatocytes were resuspended in HepatoZYME (Gibco) containing 0.1% FA-free bovine serum albumin (Sigma Diagnostics). C1-BODIPY-C12/bovine serum albumin solution was added to the hepatocytes to yield final concentrations of 2 µmol/L or 0.1%, respectively. Uptake at 37°C was stopped after 5minutes incubation by transferring 100 µL of the cells into 5 mL of ice-cold stop solution (Hank's buffered salt solution [HBS], 0.1% bovine serum albumin). Cells were pelleted by centrifugation and resuspended in 250 µL cold fluorescence-activated cell sorter (FACS) buffer (HBS containing 20 mmol/L EDTA, 10% fetal calf serum, and 1 µg/mL propidium iodine). Mean BODIPY uptake by living cells (propidium iodine negative, dead cells gated out) was determined using a FACSCalibur (Becton Dickinson, Rockville, MD).

Chapter4
In Vitro Luminescence Assays.

Millipore water was used to prepare all aqueous solutions. Incubation of CCL-1 with different metal ions ($MgCl_2$, $CaCl_2$, $MnCl_2$, $FeCl_2$, $FeCl_3$, $CoCl_2$, $NiCl_2$, $Cu(MeCN)_4(PF_6)$, $CuCl_2$ and $ZnCl_2$) was performed in 50 mM Tris buffer at pH 7.4, with 5 mM GSH and 5 µM of TPA-luciferin. At the end of the incubation, 100 µl each of the solution was transferred to a well of a white, opaque 96-well plate (Corning). An equal volume (100 µl) of a solution of luciferase (100 µg/ml, Promega) in 50 mM Tris buffer at pH 7.4, with 10 mM Mg^{2+} ($MgCl_2$), 0.1 mM Zn^{2+} ($ZnCl_2$) and 2 mM ATP was added and mixed well. Bioluminescent signals were measured using a Molecular Devices SpectraMax M2 plate reader at 37°C for 1 h.

Cellular Assays.

A Xenogen IVIS Spectrum instrument (Caliper Life Sciences) was used for bioluminescence imaging in all cellular experiments. PC3M-luc cells were cultured in DMEM containing 10% FBS. Prior to assaying, cells were passaged and plated (1.5×10^4 for PC3M-luc cells per well) in black 96-well plate with clear bottoms (Becton, Dickson and Company). The cells were then supplemented and incubated with $CuCl_2$ (DMEM with 10% FBS) at different concentrations for 24 h. The medium was removed and 100 µl of CCL-1 (25 µM or 50 µM in DMEM with 2.5% DMSO) was added. The plate was immediately imaged for 2 h. For chelation experiments, NS3' (200 µM final concentration in DMEM) was added before addition of CCL-1.

Imaging Exogenous Copper with CCL-1.

FVB-luc[+] and L-Luc mice were given intraperitoneal (i.p.) injections of the following sets of compounds and/or vehicles under anesthesia (isoflurane inhalation 2-3%). FVB-luc[+] mice were injected with CCL-1 (0.2 µmol in 25 µL DMSO) after i.p. injection of vehicle (50 µL PBS), $CuCl_2$ (3 mg/kg in 50 µL PBS)), or both $CuCl_2$ (3 mg/kg in 50 µL PBS) and ATN-224 (5 mg/kg in 50 µL PBS). Injection of $CuCl_2$ and ATN-224 were performed 2 h and 10 min prior to injection CCL-1, respectively. L-Luc mice were injected (i.p.) with CCL-1 (0.1 µmol in 25 µL DMSO) after i.p. injection of vehicle (50 µL PBS), $CuCl_2$ (3 mg/kg in 50 µL PBS) alone, both $CuCl_2$ (3 mg/kg in 50 µL PBS) and ATN-224 (5 mg/kg in 50 µL PBS), or ATN-224 (30 mg/kg in 50 µL PBS) alone. Injections of $CuCl_2$ or ATN-224 alone were performed 2 h prior to injection of CCL-1. Mice injected with both $CuCl_2$ and ATN-224 were injected 2h and 10 min prior to injection of CCL-1, respectively. Following injection of CCL-1, mice were transferred to a Xenogen IVIS Spectrum (Caliper Life Sciences) and imaged for 60 min under isoflurane anesthesia (2%).

Tissue Harvesting and Inductively Coupled Plasma Mass Spectrometry (ICP-MS).

Mice were heavily anesthetized, euthanized by cervical dislocation, and slowly perfused with PBS (10-25 mL). Following perfusion, tissues were harvested and immediately placed on dry ice in cryotubes and stored in -80 ºC until analyzed. For ICP-MS analysis, 20-100 mg portions of the harvested tissues were digested in concentrated nitric acid (100 mg/mL HNO_3, BDH Aristar Ultra) at 90 ºC for 2 h in 1.5 mL tubes (Sarstedt) with small holes poked in the caps. After overnight incubation at room temperature, samples were diluted into 2% HNO_3 and doped with a gallium internal standard (Inorganic Ventures, 20 ppb final concentration). The copper content was determined by measuring [63]Cu using a Thermo Fisher iCAP-Qc ICP-MS in Kinetic Energy Discrimination (KED) mode with the He flow

set to 4.426 mL/min. Measurements were normalized to a standard curve of known copper concentrations doped with 20 ppb Ga. The standard curve was diluted from CMS-5 (Inorganic Ventures).

Chapter 5
General Material and Methods.
Caged D-cysteine peptides DEVD-(D-Cys) and GGR-(D-Cys) peptides were custom made by Protein and Peptide Chemistry Facility (PPCF) - UNIL (University of Lausanne, Switzerland). Nitriles 3 was synthesized according to the reported procedure.[176] The rest of the chemicals used in the study, were obtained from the following commercial sources and used without further purification. D-cysteine and NH_2-CBT were purchased from Sigma-Aldrich (St. Louis, MO). L-cysteine was purchased from Alfa Aesar (Ward Hill, MA) and OH-CBT from ABCR GmbH (Karlsruhe, Germany). Luciferase was purchased from Sigma-Aldrich (St. Louis, MO), ATP was purchased from AppliChem GmbH (Darmstadt, Germany) and caspase 3 was kindly provided by Dr. Salvesen at Stanford University, CA.[192] Luciferase buffer used to quantify the amount of luciferin formed during incubation was prepared as following: 60 µg/mL of luciferase (Sigma-Aldrich (St. Louis, MO)) in 50 mM Tris buffer, pH 7.4, with 0.1 mM $ZnCl_2$, 2 mM ATP and 10 mM $MgCl_2$. 60 µg/mL luciferase in 0.1M Tris-HCl pH=7.4, 2 mM ATP, and 5 mM $MgSO_4$. All *in vitro* and cellular studies were performed in clear bottom black 96 well plates which were purchased from Becton Dickinson and Company (Franklin Lakes, NJ). Spectramax Gemini (Molecular Devices, Sunnyvale, CA) or IVIS Spectrum camera (PerkinElmer, Alameda, CA) were used to measure the amount of BLI signal production.

In vitro formation of D-luciferin and D-aminoluciferin in physiological solutions
23 µL of a NH_2-CBT solution (50 mM in MeOH) was added to either 50 µL of D-cysteine (16 mM in PBS), L-cysteine (16 mM in PBS), or 50 µL of PBS solution and allowed to incubate at room temperature for 1 h. After incubation, 40 µL of the resulting solution was added to 80 µL of luciferase buffer (60 µg/mL luciferase in 0.1M Tris-HCl, 2 mM ATP, and 5 mM $MgSO_4$) in a 96-well plate immediately before reading bioluminescence emission using a Spectramax Gemini (Molecular Devices, Sunnyvale, CA). Bioluminescence signal was measured every 22 s for 2 h.

Cellular Experiments.
IVIS Spectrum Camera (PerkinElmer, Alameda, CA) was used for bioluminescent imaging in all cell experiments. SKOV-3-Luc-D3 cells (PerkinElmer, Alameda, CA) were cultured in McCoy's 5A medium containing 10% FBS, 1% GlutaMAX and 1% Penicillin/Streptomycin mixture. Cells were passed

and plated (1 x 10^4 cells/well) in a black 96-well plate with clear bottoms (Becton Dickinson and Company, Franklin Lakes, NJ). 48 h after the seeding the growth medium was removed and the cells were first washed with 200 μL of PBS, followed by incubation for 5 min with 100 μL solution of D-cysteine or L-cysteine in PBS (150 μM, 15 μM or 1.5 μM) or PBS along (control). After a second addition of 100 μL solutions of OH-CBT, NH_2-CBT or D-luciferin in PBS (150 μM, 15 μM or 1.5 μM), the cells were immediately placed in IVIS Spectrum and the plate was imaged for the duration of 1 h with one image acquired every minute. Observed BLI signal was quantified using region-of-interest (ROI) analysis available on Living Image software (PerkinElmer, Alameda, CA).

Bioluminescent caspase-3 assay with DEVD-(D-Cys) peptide and amino-CBT.
Caspase-3 was purified and characterized following the reported procedure (kindly provided by Dr. Salvesen at Stanford University, CA).[108] Different concentration solutions of capsase-3 (50, 100 and 200 nM) were prepared in caspase buffer (100 mM HEPES pH 7.4, 0.1% CHAPS, 1 mM EDTA, 10 mM DTT, 1% sucrose) and were aliquoted in a 96 well-plate (50 μL caspase-3 solution/well). The plate was incubated at 37 °C for 15 min in order to preactivate the caspase. Followed preactivation, 50 μL of a 800 μM DEVD-(D-Cys) solution or 50 μL of a 800 μM D-Cys solution in caspase buffer was added in each well and the plate was incubated at 37 °C for 3 h. After the incubation, 100 μL of a 400 μM solution of NH_2-CBT in MeOH was added to each well and the plate was incubated for another 1 h at 37°C. Luciferase buffer (60 μg/mL luciferase in 0.1M Tris-HCl, 2mM ATP, 5 mM $MgSO_4$) was freshly prepared and aliquoted in a second 96-well plate (115 μL/well). 5 μL of the resulting caspase-3 containing solutions was quickly added to luciferase buffer immediately before reading bioluminescence emission using a Spectramax M5 (Molecular Devices, Sunnyvale, CA). Bioluminescence signal from the plate was measured every 5 min with 500 ms integration time for the duration of 2 h.

Animal experiments in FVB-luc+ mice.
IVIS Spectrum Camera (PerkinElmer, Alameda, CA) was used for BLI imaging in all animal experiments and the resulting data were processed using Living Image software (PerkinElmer, Alameda, CA). All solutions were prepared in sterile DMSO obtained from Sigma-Aldrich (St. Louis, MO) and PBS purchased from Life Technologies Corporation (Paisley, UK). Prior to injection and during the imaging procedure mice were anesthetized by inhalation of isoflurane (Phoenix, St. Joseph, MO), that was premixed with medical grade oxygen purchased from Praxair (Danbury, CT). To study split luciferin ligation reaction in living female FVB-luc+ mice, the animals were IP injected with either OH-CBT (5 mice per group); NH_2-CBT (5 mice per group); D-Cysteine and OH-CBT in equimolar

concentrations (1:1) (5 mice per group); D-Cysteine and NH_2-CBT in equimolar concentrations (1:1) (5 mice per group); D-Cysteine and OH-CBT in 1:10 ratio (5 mice per group); D-Cysteine and NH_2-CBT in 1:10 ratio (5 mice per group); and D-luciferin (5 mice per group). All injections were done at one equivalent of 0.267 mmol/kg concentration in either 100 μL of PBS for D-Cysteine or D-luciferin and 20 μL DMSO for OH-CBT or NH_2-CBT. The time period of 3 min between IP injection of D-cysteine and CBT derivatives was respected and the animals were imaged right after the second injection with CBT. The animals injected with D-luciferin were imaged right after the injection with the compound.

Real time non-invasive imaging of caspase 3/7 activities in FVB-luc+ mice.
Female FVB-luc+ mice (4 mice per group), were anesthetized with isoflurane and injected IP with either lipopolysaccharides (LPS) purchased from Sigma-Aldrich (St. Louis, MO) at concentrations of 100 μg/kg in 50 μL of PBS followed by injections of D-(+)-Galactosamine hydrochloride (D-GalN) obtained from AppliChem GmbH (Darmstadt, Germany) at concentrations of 267 mg/kg in 50 μL of PBS. The control group of mice was injected with 100 μL of PBS (vehicle along). Six hours after injection with combination of LPS and D-GalN or vehicle along (PBS), mice were treated IP with either DEVD-(D-Cys) peptide (22.6 mg/kg in 100 μL of PBS) plus 6-Amino-2-cyanobenzothiazole (NH_2-CBT, 6.8 mg/kg in 20 μL of DMSO) or commercial DEVD-aminoluciferin substrate (34 mg/kg in 100 μL of PBS) and imaged. A time period of 10 min between injections of DEVD-D-Cys and NH_2-CBT was respected. The mice were imaged using IVIS Spectrum and bioluminescence images were obtained every minute during the period of 1 h.

Statistical Analysis
The number of mice chosen for each experiment is based on the principle that the minimal number of mice is used to have sufficient statistical power and is comparable to published literature for the same assays performed. No animals were excluded from the analyses. Mice were randomized to groups and analysis of mice and tissue samples were performed by investigators blinded to the treatment of genetic background of the animals. Statistical analysis was performed with Excel (Microsoft) and Prism 5.0 Software (GraphPad Software). Means between two groups were compared with two-tailed, unpaired Student's t-test. Error Bars represent standard errors. In all corresponding figures, * represents $p<0.05$. ** represents $p<0.01$. *** represents $p<0.001$. ns represents $p>0.05$.